



# Qualification of a laser system for cold atom experiments with potassium in microgravity

## Bachelor thesis

for obtaining the degree  
Bachelor of Science (B.Sc.)

Humboldt-Universität zu Berlin  
Faculty of Mathematics and Natural Sciences  
Department of Physics  
AG Optische Metrologie

submitted by   Julien Kluge  
date of birth   30th January 1995  
born in       Berlin  
email         julien@physik.hu-berlin.de

primary examiner   Prof. Achim Peters, PhD  
secondary examiner   Dr. Markus Krutzik

Berlin, 9th May 2018



# Contents

<b>1</b>	<b>Quantum gravity and ultra cold quantum gases in microgravity</b>	<b>1</b>
1.1	QUANTUS collaboration	3
1.2	BLASTEK capsule at the Bremen drop tower	4
1.3	Potassium laser system	5
<b>2</b>	<b>Laser system control</b>	<b>7</b>
2.1	TBus system	8
2.2	Meerstetter temperature cards and COM Board	9
2.3	Photodiodes	11
<b>3</b>	<b>Qualification stage I: Berlin mini drop tower</b>	<b>12</b>
3.1	Data capturing	13
3.2	Drop data evaluations	19
3.3	Master laser autolock	21
3.4	Evolutionary swarm optimizing of TECs	26
3.5	Qualification results and conclusions	32
<b>4</b>	<b>Qualification stage II: Bremen drop tower</b>	<b>33</b>
4.1	Data capturing	35
4.2	Drop tests and sequences	38
4.2.1	Drop procedure	38
4.2.2	Conducted drops	39
4.2.3	Data evaluation	40
4.3	Results and conclusions	45
4.4	Future tests	46
<b>5</b>	<b>Qualification summary and outlook</b>	<b>47</b>
5.1	Summary of qualification results	47
5.2	Outlook	48
5.2.1	BLASTEK	48
5.2.2	Berlin BEC ground testbed	48
5.2.3	QUANTUS-2 dual species operation	49
<b>6</b>	<b>References</b>	<b>50</b>
<b>7</b>	<b>Appendix</b>	<b>54</b>

## List of Figures

1	Scheme of Mach-Zehnder interferometer . . . . .	2
2	Photo of the BLASTEK capsule structure and in operational form . .	4
3	Schematic of the potassium laser system . . . . .	5
4	Captured potassium spectrum . . . . .	5
5	41-potassium niveau levels . . . . .	6
6	TBus LABVIEW and .NET schematics . . . . .	9
7	Picture of the Meerstetter TEC tower . . . . .	10
8	Picture of the standing PD mount . . . . .	11
9	Model of the miniaturized drop tower . . . . .	12
10	Acceleration sensor absolute fourier spectrum . . . . .	15
11	Two hour long beat note of master lasers . . . . .	17
12	Allan deviation of master lasers beat . . . . .	18
13	Measurement of acceleration on the mini drop tower . . . . .	20
14	Feedback/error signal of falling master laser on mini drop tower . . .	21
15	Beat note of falling master laser on mini drop tower . . . . .	21
16	Autolock alignment . . . . .	22
17	Autolock position to current proportionality constant $\xi$ . . . . .	24
18	TEC fitness evolution with $h = \infty$ and $h = 1$ . . . . .	28
19	Fitness function pass of the Meerstetter-TEC evaluation . . . . .	28
20	Sample evolutionary optimization of fitness and parameters . . . . .	31
21	Meerstetter TEC evolution results . . . . .	32
22	Schematic of the Bremen drop tower . . . . .	33
24	Bremen drop tower z acceleration . . . . .	34
23	Schematic of the drop capsule . . . . .	34
25	System NTC temperatures in catapult start . . . . .	40
26	TEC temperature over catapult start . . . . .	41
27	MOPA beat frequency during flight . . . . .	41
28	MOPA feedback signals during catapult start . . . . .	42
29	PD signals during catapult flight . . . . .	43
30	Bremen drop tower capsule rotations . . . . .	44
31	Bremen drop tower capsule rotation angles . . . . .	45
32	Photo of Cold Quanta . . . . .	48
33	Miniaturized drop tower photos in plain and with BLASTEK interface	54
34	Accelerations while capsule start and impact . . . . .	55
35	Bremen drop tower capsule rotation projection . . . . .	55
36	Capsule NTC temperatures during flight . . . . .	56
37	Master laser feedback signal during flight . . . . .	56

## List of Tables

1	General data for each Bremen tower flight . . . . .	39
2	List of all used TBus Cards . . . . .	57
3	Comparison of correlation function for the autolock alignment calculation . . . . .	57

## **Abstract**

The QUANTUS-2 experiment is a testbed for dual-species atom interferometry in microgravity with potassium and rubidium inside a drop tower. While the rubidium laser system is already running and performing in atom-chip based BEC experiments, the potassium subsystem is coming towards final testing and calibration.

This thesis presents the recent progress made on qualifying the new laser system for the potassium sub-system. In the scope of this thesis over 90 drop tests on a miniaturized drop apparatus as well as six catapult starts in the Bremen drop tower with the BLASTEK capsule were conducted.

It was successfully shown to withstand the environmental conditions in the drop tower and the laser system was fully operable through all sequences. Beside that, further optimization for the optical powers is deemed necessary and is subject for future flights.

In preparation of the qualification tests, several algorithms for the system control and optimization were investigated. Firstly an automated frequency stabilization of the reference master laser. Secondly an evolutionary algorithm based on swarm optimization to acquire better temperature stabilization feedback parameters.

In final conclusion, the system is almost fully qualified and within the next tests the complete operability is expected to be achieved.

---

# 1 Quantum gravity and ultra cold quantum gases in microgravity

For the last 100 years, physics is divided between two worlds for different descriptions of nature. On the one side, the world of huge ranges and actions, dictating the movement of whole planets and solar systems, expressed in the general theory of relativity. On the other side, the microscopic regime on the scale of molecules down to elementary particles, reigned by quantum theories. And still, despite a lot of progress, no unification of these descriptions emerged so far [1].

This naturally spawns the idea of describing either theory in the framework of the other. Hereby a quantum theory lays on a far better ground in which already three of four fundamental forces reign in. Nevertheless, an observation of a violation of general relativity was still not seen till today. But neither was a validation of a quantum gravity theory although astronomical tests are conceivable [2–4]. It must also be mentioned that maybe no option listed gives a satisfactory description of our universe and even more advanced approaches like string theory, where gravity is a direct consequence through excitations of closed string-loops[5, 6], are the way to go for the future. However, either result would be phenomenal and spark a new chapter in modern physics.

One way to show a possible violation of general relativity, is to refute one of its pillars utilizing quantum mechanics[4]:

1. **Universality of free fall (UFF):** or also called *weak equivalence principle* dictates that every structureless baryonic matter in presence of a gravitational field moves in the same way, independently of the mass.
2. **Universality of the gravitational red shift:** states that all clocks, when moved through a gravitational field, are shifted the same direction and magnitude in their frequency.
3. **Local Lorentz invariance:** dictates that the outcome of small, local experiments is independent of the reference frame.

For the first two pillars, proposals exist to challenge and test these principles using cold quantum gases. The universality of gravitational red shift can be probed by creating extremely accurate clocks based on, for example, hyperfine structure transitions. This is already the very definition of our time keeping, since the second is defined by the time span of 9 192 631 770 from those transitions from the ground state level splitting of  $^{133}\text{Cs}$  [7]. Those clocks can maintain a frequency stability of  $10^{-16}$  [8] and recent developments with new Yb-lattice clocks approach an even better stability of  $10^{-18}$  [9]. These improvements can serve future tests and lead to an even more precise result[10].

For the context of this work, the second pillar is the most relevant as the experiments described here aim at providing a first step towards tests of the UFF with quantum gases. It was shown early in 1975 that neutron matter waves and later cooled atom clouds can be used to measure the acting acceleration on those ensembles[11–13]. To judge a possible violation of the UFF, a parameter called *Eötvös ratio* can be introduced[14] with:

$$\eta_{A,B} = 2 \frac{a_A - a_B}{a_A + a_B} \quad (1)$$

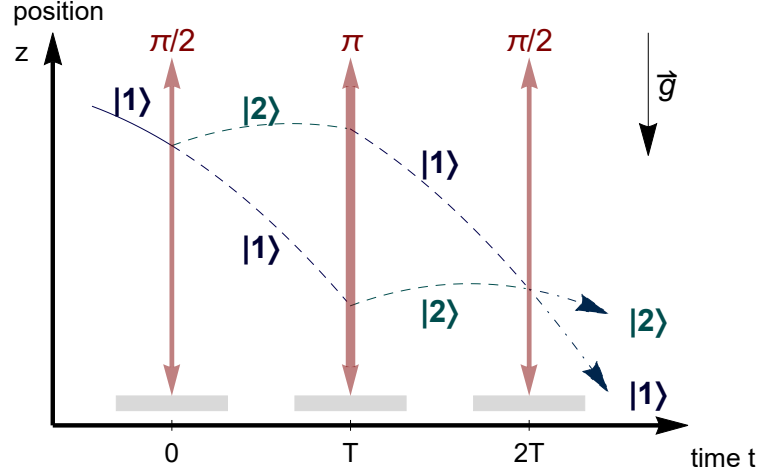


**Figure 1:** Scheme of a Mach-Zehnder type interferometer with two superimposed states  $|1, \mathbf{p}\rangle$  and  $|1, \mathbf{p} + \hbar \mathbf{k}_{\text{eff}}\rangle$ . Figure adopted from [17].

where  $a_A$  and  $a_B$  are the accelerations of two different test masses. If the UFF holds, the numerator of (1) vanishes and therefore  $\eta_{A,B} \equiv 0$ . For a violation on the other hand, the ratio must be unequal zero. The most recent test, with traditional test masses (Titanium and Platinum) on a satellite, confirmed the UFF with a precision of  $\eta_{\text{Ti,Pt}} = (-1 \pm 9(\text{stat}) \pm 9(\text{syst})) \times 10^{-15}$  [15]. When using quantum gas experiments, cold atom clouds with different atomic species can be used to probe this ratio in a Mach-Zehnder type matter wave interferometer which acts analogous to a light interferometer. In this, the wave character can be described with the de-Broglie wavelength. Beam splitter and mirrors are implemented with  $\pi$  and  $\pi/2$  light pulses (see Fig. 1). This is often referred to Bragg atom interferometry wherein a superposition of two momentum states  $|1, \mathbf{p}\rangle$  and  $|1, \mathbf{p} + \hbar \mathbf{k}_{\text{eff}}\rangle$  is created [13, 16]. After the clouds moving through the interferometer arms and creation of the reconstruction, a phase shift can be measured which is equal to

$$\Delta\Phi = k_{\text{eff}} g T^2 \quad (2)$$

Hereby, the  $\mathbf{k}_{\text{eff}} = \mathbf{k}_1 - \mathbf{k}_2$  is the effective wave number formed by the two propagating beams,  $T$  is the separation time and  $g$  is the acting acceleration which can be calculated by measuring  $\Delta\Phi$  with a known  $k_{\text{eff}}$  [17]. The sensitivity can be derived [18] with

$$\Delta a = \sqrt{\frac{2}{N C g k_{\text{eff}} T^2}} \quad (3)$$

while  $N$  being the atom number and  $C$  the interferometer contrast. It can be seen, that increasing the separation time gives a significant increase in sensitivity as well as for atom number and effective wave vector. The most beneficial change however, is a long separation time because the inverse square proportionality. To help with this, the experiment can be conducted in falling reference frames. This is the advantage of doing experiments in microgravity/weightlessness.

For long interrogation times  $T$  and high beam splitter efficiencies a cloud with low ballistic expansion rate is required. This can be reached with ultra cold atom ensembles. An ideal situation is reached with a Bose-Einstein condensate (BEC) [19].

In this, the atoms all settle in a common ground state. To enable this, all atoms must have the same quantum state which is prohibited for fermions by the Pauli-principle. Therefore the atoms must have a boson character. This limits the choice of isotopes usable in such experiments. The condensation occurs when the thermal de Broglie matter-wavelength

$$\lambda_{dB} = \frac{h}{\sqrt{2\pi m k_B T}} \quad (4)$$

expands such that it reaches a magnitude of the typical interatomic distance  $\sqrt[3]{V/N}$ . Combining this with equation (4) yields necessary temperatures for common atoms in the regime of  $T_{BEC} \approx 10^{-7}$  K. Reaching such low temperatures requires an advanced cooling mechanism. For atomic clouds, laser cooling is a rapid method for realizing this. It uses the principle of light atom interaction of momentum transfer. To only select a certain velocity class, the light frequency is altered to match the doppler shifted, thus velocity dependent, energy levels of a hyperfine splitting ground state. With the help of a quadrupole magnetic field and the resulting Zeeman splitting, this can be broadened even further and additionally implement a trap (MOT: magneto optical trap). The detailed driving of transitions is part of different cooling schemes[20, 21]. The retransmitted photon still gives momentum back but in the average this is a vanishing contribution. Therefore only the velocity gain due to the laser light is leading to a manipulation of the overall cloud momentum distribution. This state, called optical molasses, can cool the atoms down to the recoil velocity of a single photon momentum transfer. Typical temperatures of this are in the range of  $T_{OM} \approx 10^{-5}$  K. To further cool and reach Bose-Einstein condensation, an evaporative approach is applied. Hereby the property of gases having a Maxwell-Boltzmann velocity distribution is exploited. In this, the fastest atoms (long range wing of the distribution) are removed from the cloud with a radio frequency transition. This happens nearly interaction free. Subsequently the cloud rethermalizes and the average temperature sinks. This, however, comes with loss of atom numbers which is undesired. Afterwards the number of atoms can still be up to  $N \approx 10^6$  [22].

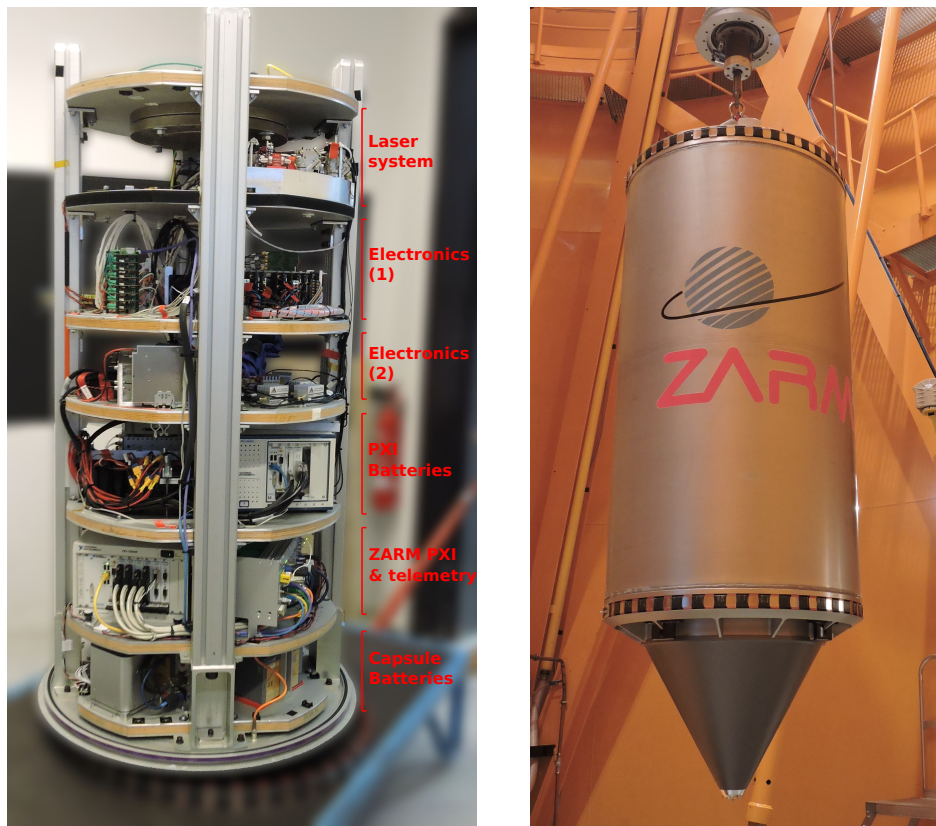
## 1.1 QUANTUS collaboration

QUANTUS (abbreviation for: **Q**uantengase **u**nter **S**chwerelosigkeit - *quantum gases under weightlessness*) is a collaboration of multiple universities and research institutions in a combined effort, of studying methods and experiments for ultra cold atom interferometry. Within this, the experiments are divided in several ventures. QUANTUS-1 is a drop tower capsule, already operating, and producing BECs with  $^{87}\text{Rb}$ . It was the first of its kind and provided a proof of concept for the experiments and also firstly used magnetic lensing with it[23]. Its successor, QUANTUS-2, aims for dual species atom interferometry with  $^{87}\text{Rb}$  and  $^{41}\text{K}$  and is the integral part of this thesis. It is already performing in atom chip based BEC experiments and is able to be dropped and catapulted in the Bremen drop tower[22, 24]. The scope of this work is the qualification of the potassium laser sub-systems whereas the rubidium part is assembled and fully works already. The third venture, is trying to mount the experiments onto a sounding rocket for extreme prolonged interrogation times. This project is called MAIUS (**M**ateriewellen**i**nterferometrie **u**nter **S**chwerelosigkeit



- *matter wave interferometry under weightlessness*). The first of three planned missions started on the 23th of January in 2017 and produced the first rubidium based BEC in space[25]. The next start will incorporate a dual species apparatus with an additional potassium system, with knowledge gained through QUANTUS-2 and aim for the first determination of the  $\eta_{\text{K,Rb}}$  Eötvös ratio in space.

## 1.2 BLASTEK capsule at the Bremen drop tower



(a) Photo of the BLASTEK capsule structure without the outer hull. (b) Photo of the BLASTEK capsule in operational mode.

**Figure 2:** Photo of the BLASTEK capsule structure (left) and in the drop tower attached to the winch (right).

BLASTEK (**B**erliner **L**asersystem **T**estkapsel - *Berlin based laser system test capsule*) is a dedicated capsule for preliminary tests of laser systems for Bremen drop tower operation. It has been utilized to qualify the rubidium part of the QUANTUS-2 experiment. Now its used for the same qualification of the new potassium subsystem in the scope of this thesis. BLASTEK itself is a catapult-able capsule (see *Fig. 2a* and *Fig. 2b*) for the Bremen drop tower. It is made up of several different layers were each has a specified tasks. The topmost configurable level, contains the laser system to qualify. The next levels are dedicated for various electronic components for controlling, monitoring and running the lasers. Details are given later in the according chapters for the Bremen drop tower. Until finishing of this thesis, the capsule made six successful catapult starts. Thereby the whole system could be almost completely qualified. The full operational state is expected to be reached in a few more starts scheduled for this and upcoming months.

### 1.3 Potassium laser system

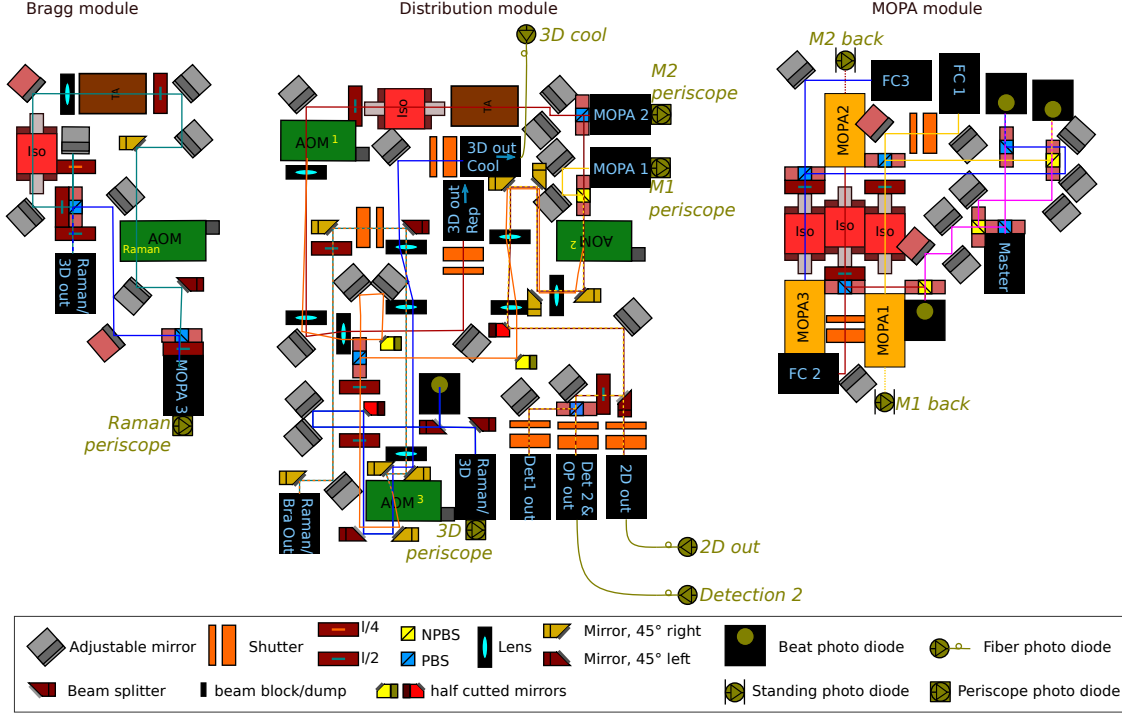


**Figure 3:** Schematic of the potassium laser system. The three parts are in order: Raman/Bragg Module (left), distribution module (middle) and MOPA module (right). The photodiode schematic is also shown here. This figure was taken and adapted from [Ref. \[26\]](#).

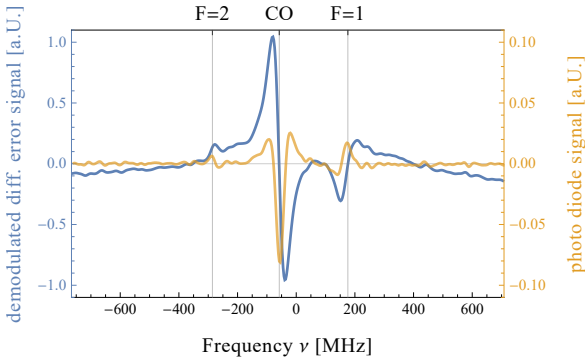


**Figure 4:** Spectrum of potassium as captured by the electronics. The optical transitions  $F = 1 \rightarrow F'$  and  $F = 2 \rightarrow F'$  as well as the crossover (CO) peak can be observed.

The potassium laser system is divided into three distinct parts fitted into a semicircle. The other half is allocated for the rubidium part with the same form factor. Both sections then form a circle which can be placed into the drop capsule. A schematic of the whole system can be seen in [Fig. 3](#). Additionally, a master laser, based on a doppler free frequency modulation, saturation spectroscopy schematic, is located inside the capsule and interfaced via optical fibers onto the board.

**MOPA board** The first module is the MOPA board which houses the lasers for the experiment. Each of them is a DFB master oscillator power amplifier built by the Ferdinand-Braun-Institute [\[27\]](#). The bench consists of three parts: the master oscillator (MO), an isolator, to prevent back scattered light to

enter the oscillator and last a tapered power amplifier (TA). In this configuration, light at  $\approx 766.701$  nm [28] is produced with approximately 1 W of output power. Driving optical transitions in potassium

requires advanced stabilizing mechanisms. To reach this, the master laser itself is stabilized with a PID controlling through doppler free saturation spectroscopy in a gas cell onto the  $|F = 1 \rightarrow F'\rangle$ ,  $|F = 2 \rightarrow F'\rangle$  or crossover  $|F = 1/2 \rightarrow F'\rangle$  frequencies. The observed spectrum is shown in *Fig. 4*. Three natural occurring isotopes of potassium can be used.

$^{39}\text{K}$  is the most common one with about 93.26 % natural abundance. It is followed by  $^{41}\text{K}$  with approximately 6.73 %. The third, fermionic, isotope of potassium is  $^{40}\text{K}$  and has an abundance of  $< 0.02$  % [29]. Therefore the master laser stabilization will be the most effective on  $^{39}\text{K}$  transitions which gives the highest transmission amplitude. However, for the later experiment  $^{41}\text{K}$  is used.

The stabilized light is then lead onto the MOPA board where a beat with a small part of each MOPA beam is created and measured by fast photo diodes which signal is divided, counted and reference compared to be fed into a PID controller scheme afterwards. This is an off-set lock were the beat frequency can be set to a desired value. For the sequences later, this is also necessary to drive the different cooling schemes (see i.e. *Fig. 5*). The majority of the MOPA light is then coupled into fibers. MOPA one and two are supplying the light for the distribution board. MOPA three first goes onto the Raman/Bragg board where the light is split, frequency shifted, amplified and combined and guided to the distribution board for final beam preparation.

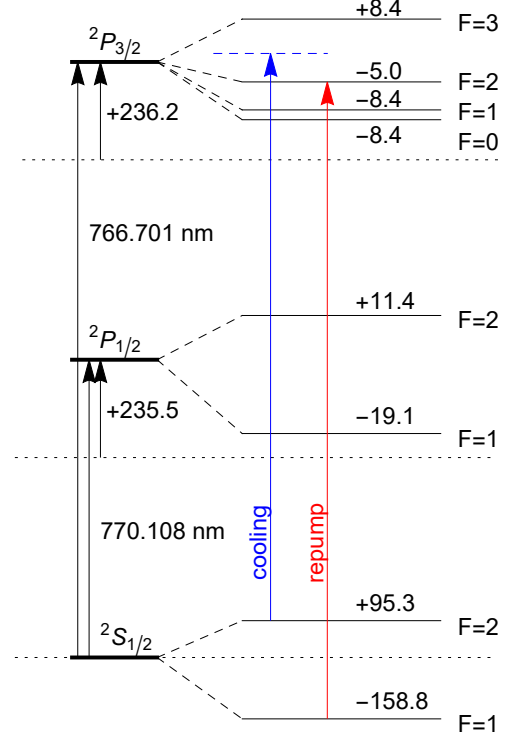


**Figure 5:** Level schematic of  $^{41}\text{K}$  with indicated cooling and repump transitions[20].

**Distribution and Raman/Bragg board** The distribution board manages the output light delivery and switching for their respective tasks. MOPA one and two are directly passed and create the beams for the two detections, the 2D cool and repump beams. With an additional amplification from a TA, extra paths for the 3D repump and Raman/Bragg is formed. The third MOPA produces solely light for the 3D cool light and uses another TA on the Raman board.

After coupling all light out of the distribution board, it is partially overlayed with the rubidium system beams and forms the final light supply for the experiment.

---

## 2 Laser system control

The control computer for the laser system must meet strong requirements. It must not only be able to withstand the forces in the drop tower but also supply real time response time frames. This rules out many widely common systems where minimum responses lie in the millisecond regime. Secondly the power consumption is limited by the capsule batteries which provide power to the system, from control computer to MOPA lasers. To fulfill those requirements a commercial real time system computer (*NI PXI-8101*) in a chassis (*NI PXI-1036DC*) was used [30, 31]. This solution houses a dual core 2 GHz processor with 1 GB of ram, a real time OS and inbuilt devices including a hard drive and many peripheral interfaces. Without any add-in consumers the maximal power input is rated with approximately 45 W. It has to be noted that all the components listed above are rated for accelerations  $a_{max} < 30\text{ g}$  peak for less than 11 ms. Although this is exceeded in the experiments, the computers never failed to work and are observed to function reliably under drop tower conditions. Additionally a card with a field-programmable gate array (FPGA: *NI PXI-7854R* [32]) was used which takes care of the digital interface link to the TBus control hardware described in the next chapter. It can also be used for creating digital triggers and timing signals which will be later used in the final experiment. The FPGA runs at a frequency of 50 MHz and therefore allows for a time resolution of 20 ns. Nevertheless the TBus link was reduced to 10 MHz to yield a more reliable communication.

The PXI was controlled by a laptop computer which is connected through the ethernet port on the PXI. Communication thus flows through TCP. This was realized with a direct LAN on ground and later with a common connection through Wi-Fi in the drop tower. The control program, written in LABVIEW, runs on the PXI while the laptop manages the program execution and provides a visual interface. For the photodiode measurements and TBus stack toggling, a data acquisition card (DAQ) (*PXI-6259* [33]) with the appropriate hardware was installed. It allows for 32 analog inputs, 4 analog outputs and 48 digital IO lines. The photodiodes were connected from the transimpedance amplifier to the analog inputs. The TBus toggle was realized by utilizing a digital channel as a TTL signal switch for a power distribution board. It housed the two power connections for each TBus stack side. The digital lines were also used for detecting GPIO signals from the temperature controller. This allowed for the evolutionary optimization of reading out the error states and thus implementing safety mechanisms.

To allow for extensive data recording but saving space on the onboard SSD, a database infrastructure was created. It allowed for continuous data capturing in case of errors or to have a lookup possibility in the future for past measurements. For this a local database on the control laptop was set up. For an efficient handling and storage of the data streams a time series database was chosen. The choice fell on *InfluxDB* since it was already successfully used in MAIUS. With the according Front-End web service (*Grafana*), a full data display for any time could be established. This has the advantage of being able to access the data over the internet. Also a rough experimental control could be shown to work which currently acts as a way of an emergency shut off for the experiment.

## 2.1 TBus system

The TBus (developed and built by Thijs Wendrich, Leibniz Universität Hannover) system is a customizable electronic control device which consists of a hardware and software component. It provides most of the functionality for the laser system and gets its commands through a hardware interface which is driven by the experiment software. This program runs on the PXI computer which is itself controlled by a laptop.

The hardware part is called stack and is built by connecting dedicated cards together. These cards all have a respective task and can communicate with each other via  $2 \times 20$  analog and  $2 \times 32$  digital channel interface. Some of these are also used to provide different voltages and timed triggering signals. Every stack contains at least two mandatory cards: an interface to the control computer and a power supply. A list of the used stack in BLASTEK can be found at [Tab. 2](#) in the appendix. The interface can be made with four different possible adapters: Ethernet, FPGA, PC-104 and USB. For testing purposes a USB interface was used while the BLASTEK capsule runs with the FPGA which was readily supported by the PXI.

The software is divided into two components. The first is the hardware-software transmit library. It changes according to the used adapter and takes care of sending and receiving data to and from the stack. The second one provides the data generation, bundling and formatting. The system configuration is realized via xml description files. Every card belongs to a corresponding file and the whole stack has a listing xml to combine all those hardware descriptions. This mainly contains so called registers which are like function calls from or to a TBus card. Calling a register runs in two steps. The second software component registers the function call, matches this with a known xml configuration and proceeds to create the necessary data buffer for this. Then the execute command from the first library uses this data buffer and sends it via the given interface to the stack. For reading operations there is another function to request data back from the hardware which then gets decoded by the second library into a readable format. This procedure can vary a bit between the different interfaces.

For BLASTEK, the electronics stack had to be divided in different parts. This was necessary or else the maximum current ratings of the bus would have been exceeded. Therefore the stack was split into to equal parts in regard to their power consumption. Then a joint was added in the split where the power lines were removed. For each part a power supply card was build in. The interface card was still connected to all cards since the joint only disconnects the power but still connects the data channels. This successfully allowed to drive the stack with two separate power supplies.

**Used TBus cards** For the full experiment structure, seven different cards were needed. This includes the FPGA interface card for the communication with the control computer. Also required are two power supply cards (see above) to provide the current in multiple, different voltages. A frequency card controls the laser frequency stabilization from the beat note signal of master laser and MOPA. It also allows applying a scanning current to capture the potassium spectrum of the master. The current driver cards provide the laser currents. They can be interfaced on the hardware side with the frequency card to process the feedback signals. A shutter card takes care of driving the shutter flags and can be triggered for a pre initialized



sequence. Two DDS (direct digital synthesizer) cards producing the radio frequency signals for the AOM frequency inputs. A single NTC capture card serves as a fast analog measurement device for up to 32 NTC temperature sensors.

**Software Layers** While the capsule experiment uses the FPGA interface for the hardware-software communication, a USB adapter was used for testing purposes. This allows for a fast and reliable trial environment. The software back-end was chosen to be .NET as a widely known and used runtime. To provide a simple software

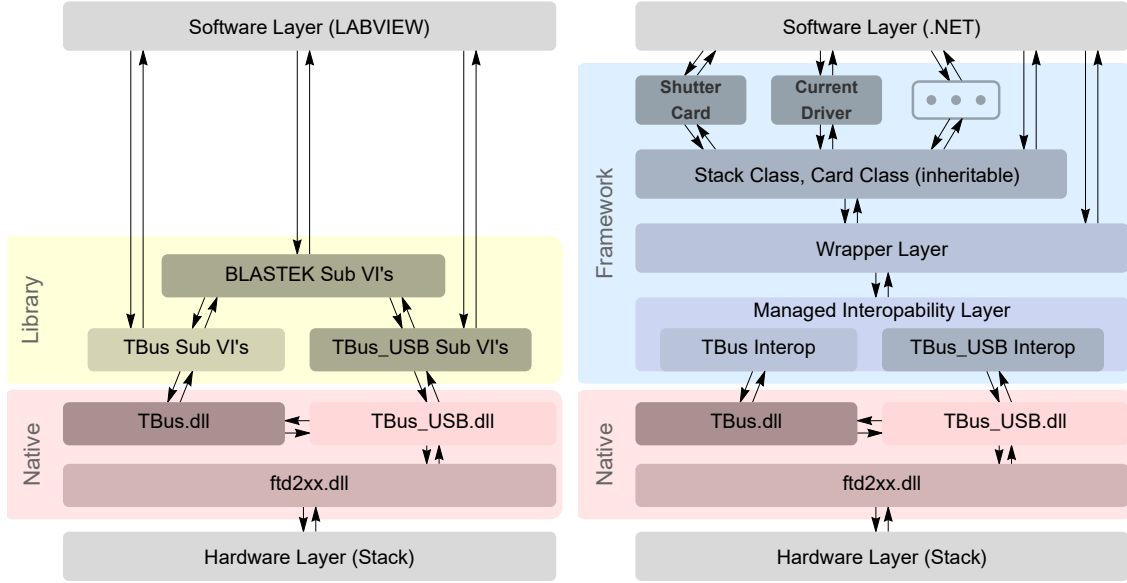


**Figure 6:** Schematics to compare the LABVIEW software libraries (left) to the .NET framework (right).

interface and decrease development time a framework was created. It was utilized with a full object oriented programming approach and is therefore very modular and versatile. The native TBus libraries, developed and created by Thijs Wendrich, were wrapped in an interoperability layer which stripped away implementation details like converting identifiers to a fixed sized, indexed data buffer or casting to the right data types. It was then enclosed by a wrapper object which made it more compact and easier to access certain operations like sending a register and collecting the resulting data from the bus. Then multiple higher abstraction stages separated unique tasks into single, compact stages. This made it possible to bundle long and complex procedure into short, highly abstracted methods while retain the possibility of low level actions. A schematic of the framework is shown in **Fig. 6** with the comparison to the LABVIEW BLASTEK library structure. Those high level methods often allowed the implementation of a single task in less than three source code lines while the same took multiple code blocks in LABVIEW or at least more data lines than necessary to a higher sub VI.

## 2.2 Meerstetter temperature cards and COM Board

The DFB diode lasers exhibit a temperature dependent frequency. They are intended to serve as constant light sources, which makes temperature stabilization

necessary. To realize this, the lasers have a mounted NTC sensor and a peltier element. The peltier is driven with a current which allows to dissipate the created heat from the structure. The temperature sensor provides the control signal. This enables the application of a feedback controller to stabilize to a set temperature. The hardware consists of a single chip (*Meerstetter TEC 1091* [34]) and is provided by Meerstetter Engineering. The interface is given via simple terminal strips to the NTC sensor and peltier element. The supply voltage can be chosen variable and is later provided by the capsule systems.

A total of seven controller is built into the system in a tower like structure as shown in *Fig. 7*. Three chips control the MOPA lasers, two the tapered amplifier, one stabilizes the master laser while the last one heats the gas cell in a simple constant current mode. To communicate with the TECs and records the temperature data streams, multiple options were used. For the mini drop tower the simple USB connection was utilized because only two chips had to be monitored. For the evolutionary optimizing measurements, described later in this thesis, the programmable GPIO digital pins were used. This allowed for easy detection of error states and other kinds of features. For the qualification tests in the Bremen drop tower a more advanced technique was necessary to record all chips except the gas cell heating one. This was implemented a dedicated communication board (COM board). This board has a small XPort computer (LANTRONIX XPort Pro [35]) on top which was able to receive TCP packets and convert them to RS-484 serial protocol commands. Those commands were converted by a micro controller to RS-232 and sent parallel to all TECs. The chips could be addressed separately by assigning an address which was used by the RS-232 messages. Although broadcasting was possible, it was never used. The XPort computer was then connected to the capsule LAN and could be used over TCP from the PXI. This allowed for reading out all Meerstetter chips and record their reactions in drop sequences.

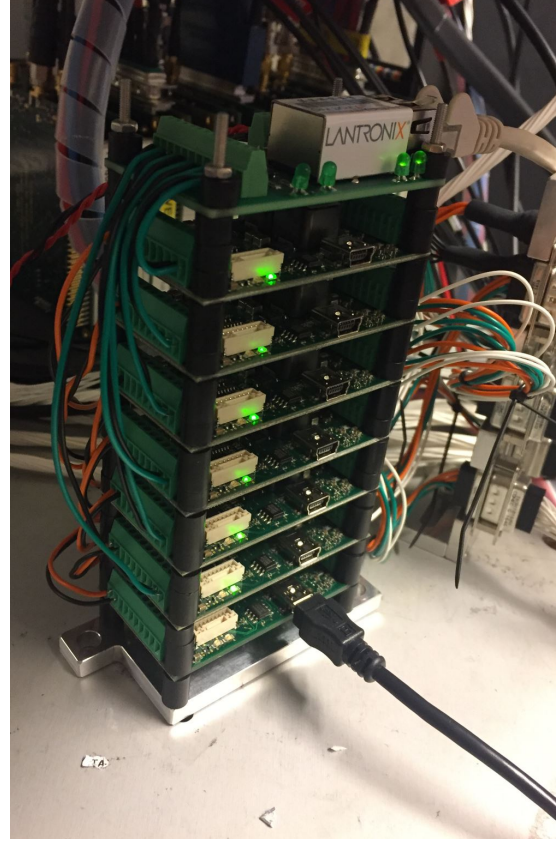


**Figure 7:** The seven TEC in their tower configuration mount as used in BLASTEK. On top sits the COM Port with the small XPort computer. The power supply is marked in orange-black cables while the green-black ones are the RS-232 serial interface with the COM board. The last TEC is temporarily connected via USB.

## 2.3 Photodiodes

To monitor the light power through the whole system multiple photodiodes are used. The fast HAMAMATSU diodes (G4176-03[36]) are used for the beat note of MOPA and master laser and their signal is sent to the frequency controller card. For power monitoring, where slower response times are sufficient, Thorlabs FDS100 photodiodes[37] are used. measurements. To realize this over the wide span of magnitudes of power, a transimpedance amplifier was used. This allowed reading out 16 diodes at four selectable sensitivities for each channel. The amplified signal was then fed in the analog break out box to be recorded.

The whole setup allowed for estimating an upper bound of the bandwidth of the diode with

$$f_{BW} = \frac{1}{2\pi R_L C_J} \quad (5)$$

with  $C_J$  being the given diode capacity and  $R_L$  the load resistance determined by the amplifier setting. This yields an interval of approximately 6.6 kHz up to 6.6 MHz. With the rise time being  $t_R = 0.35 f_{BW}^{-1}$  we get a worst case result of  $t_R \approx 53 \mu\text{s}$  which is more than enough for our purposes because typical interesting time spans in the drop tower are from second intervals down to milliseconds. Real rise times are even less than these values since the diodes are also biased which again increases the bandwidth.

Although the incident light power can be calculated with

$$P = \frac{V_0}{\Re R_L} \quad (6)$$

with  $\Re \approx 0.45 \text{ A/w}$  being the responsivity, the diodes were directly calibrated instead. The diodes were distributed in the system with three different mounting

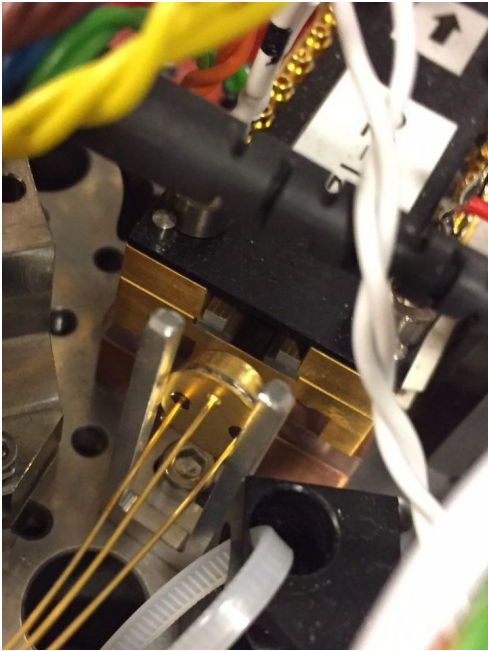


**Figure 8:** The standing mount for the slower photodiode behind a MOPA with a photodiode in place.

methods (see *Fig. 3*). Two of them were standing holders behind MOPA 2 and 3 as seen in *Fig. 8*. They used the fact that the MOPA DFB diodes emitted part of the light at the back which exits the laser unimpeded. This can be detected for output power monitoring. Another mounting method was to mount them flat underneath some of the periscopes that were used to couple light out of the fiber. The mirrors in the periscopes for the coupling do not have a perfect reflectivity thereby a small percentage gets transmitted and can be measured. The last method fixes several photodiodes on a metal bench which also holds fiber input couplers. This allowed mounting the diodes with a fiber collimator facing towards it. An alternative to the bench was also produced which featured polarized beam splitter and two diodes. This gave the possibility of monitoring the output fiber powers and polarization in drop tower operations.



### 3 Qualification stage I: Berlin mini drop tower

As first qualification stage, a miniaturized drop tower was used. The target was to verify the ability of different parts from the laser system to work under strong accelerations ( $< 40\text{ g}$ ). The master laser was particularly investigated under those conditions and data was gathered about frequency stability during nominal laboratory conditions, free fall and deceleration due to the impact on ground. The drop tower itself is built with two strong steel rods about 1.2 m long that are connected to a base station. They are joined by a steel cuboid to stabilize the rods and provide the holding mechanism for the mini drop tower platform. The rods guided a sled where one of the capsule platforms could be mounted. Various holes were drilled into the platform so that different test objects could be securely mounted to the platform. The base was covered with foam in different, changeable thicknesses to provide the ability to adjust the duration, force on impact and prevent structural damage due to metal on metal hits. A winch on the ceiling allowed a setup of the platform for the halting mechanism. In order to release the platform quickly and evenly, the hold and release mechanism was realized with two electromagnets on top of the tower, which were driven by a power supply at more than 1 A next to the tower. During the hold phase, the electromagnets would attract mounted holding arms on the sled. Additionally, a mechanical safety holding rod can be set to prevent accidental release. Next to the platform was the pre-built BLASTEK capsule located to provide the necessary umbilical to run experiments on the platform. Photos of the plain tower and the interfacing with BLASTEK can be seen in *Fig. 33* in the appendix. Next to the equipment needed to assess the system, an acceleration sensor was mounted on the platform. This allowed tuning the foam thickness to reach forces comparable to the Bremen drop tower. The optimal acceleration to be reached was determined[38] to approximately  $35 - 40\text{ g}$ . Despite some efforts to keep this value in most of the tests nearly constant, it was observed that small changes in position and angle of the foam lead to strong deviations from this optimum. As a result most measured values were between 30 and  $40\text{ g}$ . Those impacts nevertheless proved strong enough to disclose weaknesses in the apparatus. Therefore, the tests on the

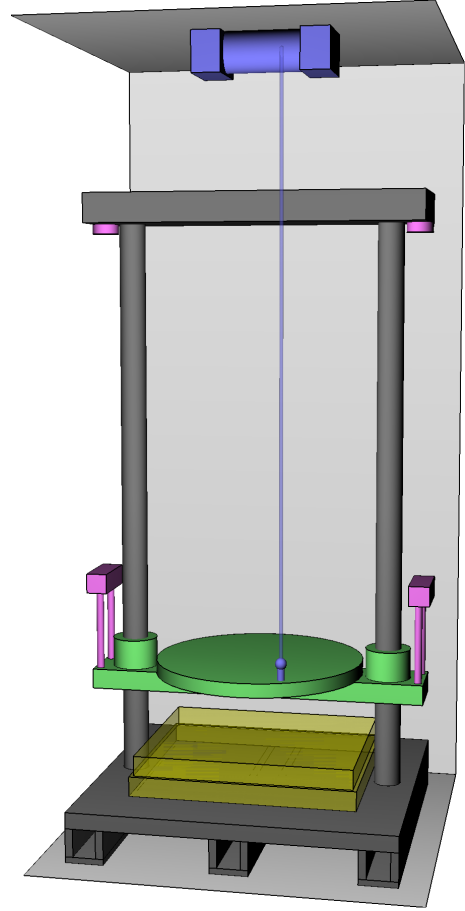


**Figure 9:** Model of the mini drop tower. Specific areas are colored in. yellow: breaking foam; green: sled and platform; magenta: magnetic holding arms and coils; blue: winch and rope

plain tower and the interfacing with BLASTEK can be seen in *Fig. 33* in the appendix. Next to the equipment needed to assess the system, an acceleration sensor was mounted on the platform. This allowed tuning the foam thickness to reach forces comparable to the Bremen drop tower. The optimal acceleration to be reached was determined[38] to approximately  $35 - 40\text{ g}$ . Despite some efforts to keep this value in most of the tests nearly constant, it was observed that small changes in position and angle of the foam lead to strong deviations from this optimum. As a result most measured values were between 30 and  $40\text{ g}$ . Those impacts nevertheless proved strong enough to disclose weaknesses in the apparatus. Therefore, the tests on the

mini drop tower fulfilled their purpose as first preparation stage for full drop tower operation. However, some of those weaknesses were exclusive to this construction and had to be remedied as far as possible. Residual deviations were ignored since they would not appear in the Bremen drop tower. Two notable faults of this were the movement of the RF cables from the BLASTTEK interface which lead to parasitic interference in the signals and the air turbulence produced by the falling platform. The first one was tried to prevent by holding and guiding the cables manually while falling and also by rigidly attaching them to their respective ends. Also cable separation between different strands helped to reduce cross talk. This dampened the shocks seen in the signals a little bit. Later on, some cables were also changed to a more shielded counterpart. The wind itself affected mostly the master lasers which lead to thermal fluctuations visible in the reference frequency. This was easily circumvented with wrapping foil around the affected parts (see [Fig. 33 b](#) in appendix).

**Experiment procedure** A typical drop on the mini drop tower can be divided into three phases. The first one was to prepare and set up the desired experiment. This meant to prepare the needed equipment for the drop. Typically this consists of starting up the power supplies, TBus, TECs, lasers, RF signal components, g-Sensor, oscilloscopes and the measurement programs. Afterwards the platform was attached to the winch and pulled to the top. The electromagnets would now be started and attract/hold the platform mounts. An additional safety rod would be put in place to prevent accidental release. The winch could then be detached and positioned in a non interfering place. The platform is now held only by the magnets and phase two comes into play with the agreement of all experimenters.

All measurement equipment (oscilloscopes, TEC recording and TBus) was turned on. In the first drops this also required a person to stand next to the tower and getting ready to hold and guide the cables before and while falling. The last action before the drop was to detach the safety rods. This marks also a *point of no return* which means that the platform has to fall even if the experiment must be aborted due to unforeseen reasons. The falling is initiated by turning off the power supply for the electromagnets. This is also coordinated with the person guiding the cables to provide a movement as smooth as possible. The coordination is necessary since the falling takes place in about half a second.

The third phase begins immediately after impact. The oscilloscopes would be stopped as well as the TBus and TEC recordings. The data are saved and gathered. A preliminary evaluation can be done in less than five minutes. A special regard was taken on the g-Sensor data to calculate the impact acceleration. This has to always be taken into account since the acceleration inevitably deviates a lot due to minor changes in the foam positions. With all three phases and all systems enabled, about two drops per hour were possible. This sped up significantly when only a single system (like the master laser frequencies) was measured and evaluated.

### 3.1 Data capturing

**Meerstetter TEC** In order to keep the output frequency of the laser diodes constant as well as provide a cooling mechanism for the amplifiers, all lasers are temperature stabilized. The hardware consists of several *Meerstetter TEC 1091*

controllers[34]. These chips use a feedback PID principle by measuring the temperature from the NTCs of the laser and providing a feedback signal to a mounted peltier element. The MOPA TEC were calibrated in their parameters with the provided standard mechanism of Meerstetter. In the beginning, the master laser TEC was also optimized with this method but it was found that the PID values obtained in this way were insufficient. Rather than doing the optimization per hand, an evolutionary algorithm was developed, tested and successfully deployed to find a better local minimum. This is further described in section 3.3.

To continuously monitor the TECs a dedicated program was written. It used the provided software interface from Meerstetter (MeCom API[39, 40]). This allowed for querying various data types from the chips over a simple USB interface. For drops, the temperature as well as the currents were recorded. Since reading from a USB stream is a blocking action, a multithreaded approach was used. This allowed for double the readout speed from two TECs. In most drops this enabled the measurement for the laser temperatures/currents of both master lasers. In some cases this was reconfigured to capture a gas cell temperature of one of the lasers.

This allowed a resolution of 55 Samples/s on average for temperature and current. Disabling one of those gave nearly two times the frequency for a single channel. Having both channels enabled gave still enough resolution ( $\geq 18$  ms) to fully resolute the impact event.

**Acceleration sensor** To create a similar testing environment to the Bremen drop tower, comparable accelerations had to be created. The assessment for this was done with an acceleration sensor (ADXL150JGQ [41]). The chip was reused from rubidium mini drop tower tests in the past and is mounted on a PCB with the appropriate driving electronics. The input voltage was provided with a simple power supply at 5 V. Measurements were made with a digital oscilloscope. This allowed for a capturing resolution of over 1 MSamples/s. It was nevertheless determined that 100 kSamples/s is enough to fully resolve all interesting events ( $\geq 10$   $\mu$ s) which also limits the produced data to evaluate. To convert the measured voltage into an acceleration, a sensitivity of  $\alpha^{-1} = (38.0 \pm 0.5)$  mV/g was given in the data sheet. Contrary to that an auto calibration scheme was introduced with the aim of improving the accuracy. The calibration exploited the fact that, while stationary, the sensor must measure a constant  $-1$  g from earths acceleration. For the scaling, another point could be measured with  $\approx 0$  g while falling. This neglects the air resistance and rod-sled frictions which is justified with the small velocities reached. The scaling factor could therefore determined with

$$\alpha = \frac{1 \text{ g}}{|U_{-1g} - U_{0g}|} \quad (7)$$

The acceleration can then be written as

$$a = \alpha (U - U_{0g}) = 1 \text{ g} \cdot \frac{U - U_{0g}}{|U_{-1g} - U_{0g}|} \quad (8)$$

The respective mean values and uncertainties for  $U$ ,  $U_{-1g}$  and  $U_{0g}$  can be calculated from the measured sample curve.

Unfortunately, the drop tower produces a lot of vibrations while falling and the sensor experiences a lot of ringing noise. To counteract this, a fourier based filter

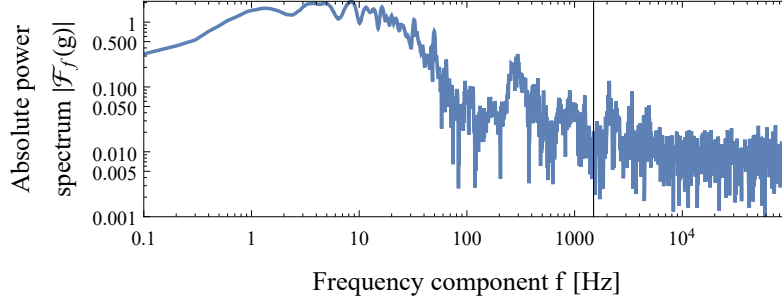


**Figure 10:** Absolute fourier spectrum of the acceleration data. The line marks the cutoff lowpass frequency. The three peaks after the cut are attributed to the vibrational noise.

was used. This approach takes the numerical fourier transformation of the data and sets high frequency bins to zero. This acts effectively as a low-pass filter. The procedure can be written in vector form as:

$$\tilde{\vec{x}} = \hat{\mathcal{F}}^{-1} \left\{ \text{diag}_n [\Theta(\sigma - n) + \Theta(\sigma + n - N)] \cdot \hat{\mathcal{F}} \vec{x} \right\} \quad (9)$$

where  $\vec{x}$  is the data vector,  $N$  the sample count,  $\Theta$  is the heaviside theta function and  $\hat{\mathcal{F}}$  denotes the fourier transformation where  $\hat{\mathcal{F}}^{-1}$  is the inverse.  $\sigma$  is the effective cut off frequency. This value has to be chosen in a way that it cuts the high frequency noise but not the desired signals. To do this, the power spectrum  $|\hat{\mathcal{F}} \vec{x}|$  can be analyzed. A calculation over experimental data can be seen in [Fig. 10](#). It shows the found cut off value in a valley. The three peaks after this line can be fully attributed to the observed noise. Everything before that is the acceleration signal. The filter can also be seen visually in action in [Fig. 13](#). The gray background is the real measured signal with noise where the blue line is the fourier filtered data. Although the noise was pretty strong which leads to high uncertainties, the fourier filter is able to extract a clean signal to assess the accelerations.

**Frequency counter** While the stationary master laser was controlled by analog rack electronics, the falling one was monitored with the TBus. This is realized through the frequency controller card. It captures and sets the laser states (free running, scanning, or actively frequency stabilized), feedback currents and error signals. Next to the normal laser control mechanism it provided the ability to measure the beat frequency.

To do this the card has a *first in, first out* mode or short *FIFO*. In this mode, the card uses the internal buffer as an indexed ring memory. As long as the data is faster read than written the data keeps consistent in this buffer. The memory allowed for 128 entries without the buffer overflowing. The card was then read out via the normal LABVIEW sub VI's and saved in a continuous csv file.

Additionally, instead of reading all desired channels separately, the frequency controller provided a so called HEX16 mode. This is an encoding scheme meant to read out all necessary data streams in a fast fashion. To employ this scheme, the card grouped all important channels in a 16 entries long enumeration. Each entry in this structure was reserved for one kind of data depending on the hardware interfacing. The values were also encoded in simple unsigned 16bit integers. This required

proper decoding techniques when evaluating the data stream. For frequencies this needed the calculation of a channel resolution. So the 16 bit unsigned integer was reinterpreted as a 16 bit signed one which requires a two's complement when the highest significant bit is set. Afterwards this can be treated as an unscaled frequency with a proportionality constant of

$$f_{scaling} = 2^s \cdot \frac{d/\tau_{gate}}{\beta} \quad (10)$$

where  $s$  denotes an applied bit-shift,  $\tau_{gate}$  the gate time where the card measured the crossings,  $\beta$  a repetition of this window and  $d$  a divider of this multiplied gate value.  $d$  is also a potency of two and could therefore be included in  $s$  but is left standing alone because those two values are separately controllable and are applied in different stages at the calculation in the card. Since this process is a continuous one, the starting index can be arbitrary within the enumeration. To obtain the absolute index, the modulo 16 of the arbitrary, returned, relative index can be applied. Otherwise it can often also automatically be determined through the structure of the values in the enumeration. Both possibilities were later employed in the main data capturing program for the Bremen drop tower while for the mini drop tower only the latter one was used.

While writing into the FIFO buffer can be seen as approximately deterministic with a fixed time interval, reading the data was not. This was not a problem for the short falling tests but provided insufficient precision for the long time measurements. To compensate this effect and create stable time recordings, timestamps were written after every buffer read out and negated. This is a reliable way of determine if a given point is content of a FIFO buffer or a time stamp. This is due to the fact that the HEX16 mode outputs only unsigned 16 bit values even if they are negative. In the evaluation the time stamps can be extracted, negated and be linearly interpolated between the given points. This is described in detail in section 4.1.

**Beat note** To measure the long and short term stability of the frequency (especially around the time of impact) from the master laser a beat note with another reference laser was implemented. For this, one master laser was mounted on the drop tower to fall while another one got fastened in the stationary capsule. The light was coupled into two respective fibers and overlayed. The mixed light was then pointed at a fast photodiode (G4176-03[36]) which then was recorded after prescaling via the Frequency card. To understand how this stability measurement works, one has to look what is detected by the diode. To do this, we can see the overlapped light beams as a sum of two cosine waves with their respective amplitudes  $A, B$ , frequencies  $f_1, f_2$  and a corresponding phase shift  $\varphi$ . The diodes senses not the direct amplitudes over time  $t$  but the absolute square of them. By applying the euler relation of sine and cosine, one can get the following identity:

$$\begin{aligned} [A \cos(f_1 t) + B \cos(f_2 t + \varphi)]^2 &= \frac{A^2}{2} (1 + \cos(2f_1 t)) \\ &+ \frac{B^2}{2} (1 + \cos(2f_2 t + 2\varphi)) \\ &+ A \cdot B \cos([f_1 - f_2] t - \varphi) \\ &+ A \cdot B \cos([f_1 + f_2] t + \varphi) \end{aligned} \quad (11)$$

This shows that there are four different resulting frequency components. Since the single frequencies  $f_1, f_2$  are extremely high in the THz regime, their effectively lowpassfiltered on the diode which cancels the three components:  $2f_1, 2f_2, f_1 + f_2$ . This leaves the photodiode to measure the frequency term  $f_1 - f_2$ , which is the frequency difference between the two master lasers. The frequency difference between the two master lasers depends on the atomic transitions that each laser was stabilized to. Two options were considered for this measurement:

- Crossover and  $F = 1, 2 \rightarrow F' \Rightarrow \Delta\nu_1 \approx 230.9 \text{ MHz} = \Delta\nu_2/2$
- $F = 1 \rightarrow F'$  and  $F = 2 \rightarrow F' \Rightarrow \Delta\nu_2 \approx 461.7 \text{ MHz} = 2\Delta\nu_1$

Despite the fact that  $\Delta\nu_2$  is greater and would therefore provide less relative uncertainty,  $\Delta\nu_1$  was chosen for the measurements. This is justified because a lock on the crossover transition is much more easy and stable since its amplitude is by far the biggest as one can examine in [Fig. 4](#). As a second lockpoint the  $F = 1$  peak was chosen as it has a higher signal amplitude and will thus provide a larger capture range which might be of advantage for this measurement. The falling laser on the drop platform was set to the crossover transition with the highest signal to noise ratio. This proved to be the most stable configuration possible. The light was experimentally captured by a fast photodiode with a ND-filter beforehand. The diode was used with a bias tee for better sensitivity. The signals were amplified by about 22 dB (ZX60-3018 amplifier) and then sent to the frequency controller.

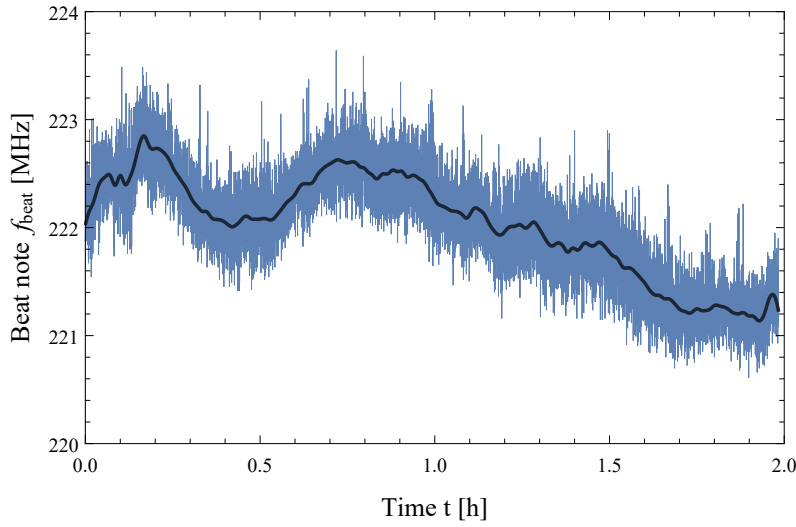


**Figure 11:** Two hour measurement of the beat note of the two master lasers at target frequency  $\nu_1$  in laboratory conditions.

The beat note was not only used to check the frequency stability while falling but also in stationary situations. This gives a rough estimate of the long term behavior of one laser. To do this, multiple hours long measurements were made where the beat was captured with a resolution of about 80 samples/s. A sample measurement with a frequency of  $\nu_1$  can be seen in [Fig. 11](#).

To estimate the frequency stability of the beat, we can use the two sample variance



also called the allan deviation  $\sigma_f(\tau)$  [42]. This gives an estimate of the RMS frequency deviations after a specified averaging time  $\tau$ . The calculation for this can be seen in [Fig. 12](#).

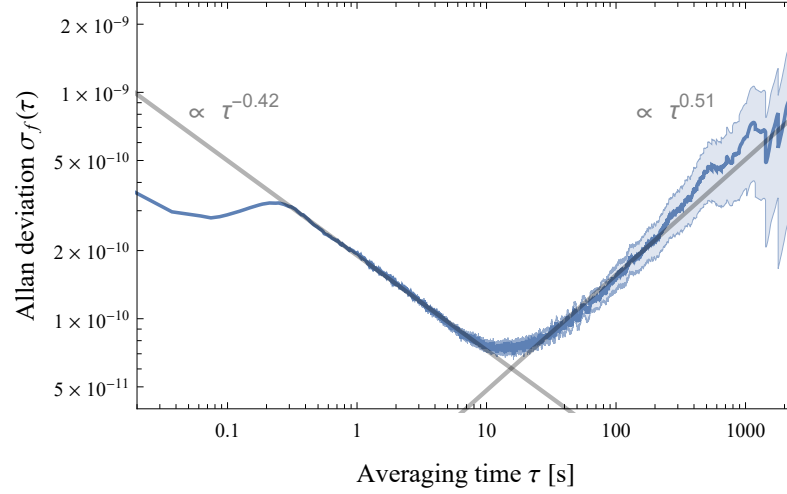


**Figure 12:** Allan deviation from the beat of both master lasers. The stationary laser was stabilized on the  $F = 1$  peak and the falling one is locked on the crossover. Two distinguishable slopes are visible with a minimum at about  $\tau_{min} \approx 16.2$  s. The enclosed area denotes the uncertainty of the deviations.

A minimum of deviation can be seen at around  $\tau_{min} \approx 16.2$  s with an variance of about  $\sigma_f(\tau_{min}) \approx 6.9 \cdot 10^{-11}$ . This shows that the master laser beat is most stable in this time regime. It also coincides roughly with the time requirement in the drop tower from approximately nine seconds. Nevertheless it has to be expressed, that this does not necessarily mean that one master laser alone exhibits this exact stability behavior but only a roughly equal one.

The slopes seen in the calculation are giving an indication of the highest contributing noise type in the respective regimes. In short time scales the noise seems to be dominated by a slope of  $\approx -1/2$  which hints to a plain white frequency noise. The rising slope has about the same value with an opposite sign and therefore indicates a random walk behavior[43].

**Experiments** In the frame of this thesis, 91 drops on the mini drop tower were conducted to qualify the system. A majority of the drops were made to find errors and problems. Most tests and specific experiments used multiple drops to either repeat it or confirm the observations. Therefore all drops can be grouped together to make a qualification timeline.

- Preliminary drops - Three drops where made before the system was fully installed to successfully test the acceleration sensor.
- **1-5:** First measurements of all measurable signals. This includes but is not limited to the master laser feedback and error signals, the beat note and the temperature controller values and currents. The laser could not be kept frequency stabilized.
- **6-8:** Optimization of the PI parameters for the laser feedback.

- **9-12:** Measurement of the locking range which was determined to around 1.9 GHz.
- **13-28:** Investigation of various possible problem sources which could prevent the lasers from keeping in lock. This includes air flow, cable cross talk and not optimized temperature controller.
- **29-31:** To circumvent bad TEC parameters new parameters were found which are too slow to control the temperature in the long run but are very stable for some seconds while dropping.
- **32-47:** Gathering of enough data to enclose the problem sources. Also parasitic feed-in signals due to movement, especially in the RF cables were investigated.
- **48-51:** Examination of a not fully heated gas cell and movement of the fiber optic cables were made.
- **52-56:** The master lasers were switched to ensure that they are not faulty. The new one had worse performance but a better correlation of observed frequency jumps and the feedback signals was seen. This hinted to a problem which is based in the lock procedure. From now on the results were often discussed with multiple people to easier find problems from the data.
- **57-60:** Another frequency counter was used to ensure that the TBus and default counter showed the right results which was subsequently confirmed.
- **66-78:** Optimization of the modulation parameters which lead to a better performance where the jumps were smaller. Some drops stayed in lock for the first time.
- **79-88:** The platform was rebuilt and some components were moved. This also had the aim to reduce the number of cables going from the platform to the stationary capsule. The temperature controllers were also mounted on the platform which marks the first test in a high acceleration environment for them. Also the influence of stray magnetic fields, ground loop problems and faulty RF components were investigated. Additionally, the first evolutionary TEC optimizing trials were done to find a single parameter set. This is described later in detail in this chapter. All these actions lead to some good drops although the problems were still not totally found.
- **89-91:** Final three drops - All three drops were good and the lasers stayed in lock. Despite this further drops were not longer possible since we noticed a damage in the left electromagnet coil. This made it impossible to do further tests. Nevertheless the coil is repaired and could be used again in the future.

## 3.2 Drop data evaluations

For evaluation of the mini drop tower environment as well as master laser the main data used comes from the last three drops as most error sources were eliminated, parameters optimized and the lasers could successfully be stabilized during the drop.



According to rough calculations the free fall time should be around  $t = \sqrt{2s/g} \approx 0.5$  s depending on foam size. This can be confirmed by looking at [Fig. 13](#) and measuring the time span of 0 g. This gives a value of around  $t = (520 \pm 7)$  ms as expected. The impact forces deviated a lot. This was attributed to changing

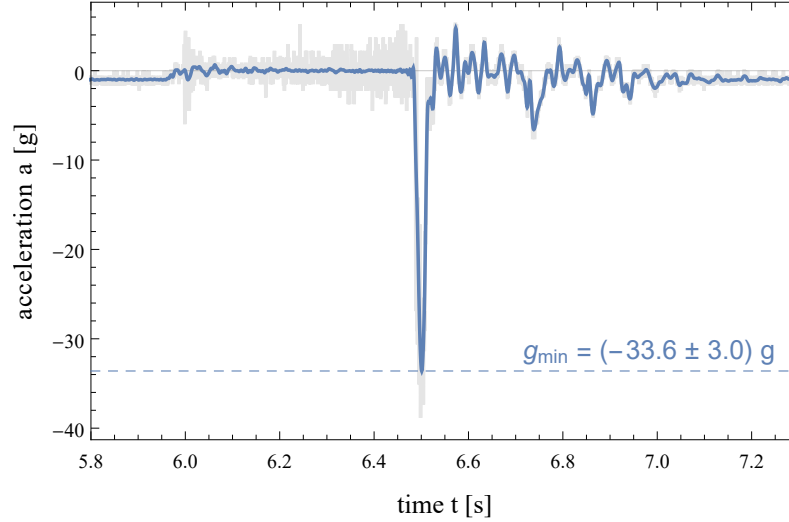


**Figure 13:** Measured acceleration on the mini drop tower. The gray background denotes the real measured data whereas the blue line represents the fourier lowpass filtered line. The impact imparted a force of around  $g_{\min} = (-33.6 \pm 3.0)$  g.

foam positions. The noisy signal as seen in [Fig. 13](#) also contributes to a high uncertainty of this value. Nevertheless all drops could be held in an interval of at least  $[-30 \text{ g}, -45 \text{ g}]$  and are therefore a good simulation for the real drop tower.

The laser reactions can also be investigated by looking at the feedback and error signals as well as examining the beat note. The desired behavior is a change in the feedback signal and a neglectable one in the error signal. With optimized parameters, the feedback loop should be able to compensate deviations in the laser frequency introduced by the drop. One can see in [Fig. 14](#) that the observations matches the expectation. However, one would also expect a constant beat since we assume the corrections are fast enough to stabilize our laser. But looking at [Fig. 15](#) reveals that this does not hold. We see a clear deviation in the average beat note of approximately half a megahertz. Nevertheless this is less than the typical periodical deviation also seen which is caused by the PI locking parameters and the temperature controllers. This noise is also seen in the feedback signal and correlates strongly with the beat deviations. Until now this is still a subject of ongoing optimizations and can also later on be seen in the Bremen drop tower data. The stationary master laser was observed to be very stable which is not a surprising result since the fall does not impede any influence onto it. This concludes that the majority of deviations in the beat are caused by frequency changes in the falling laser.

This data successfully showed and assured the ability of the master laser and TEC to withstand the occurring forces on drop tower operations.

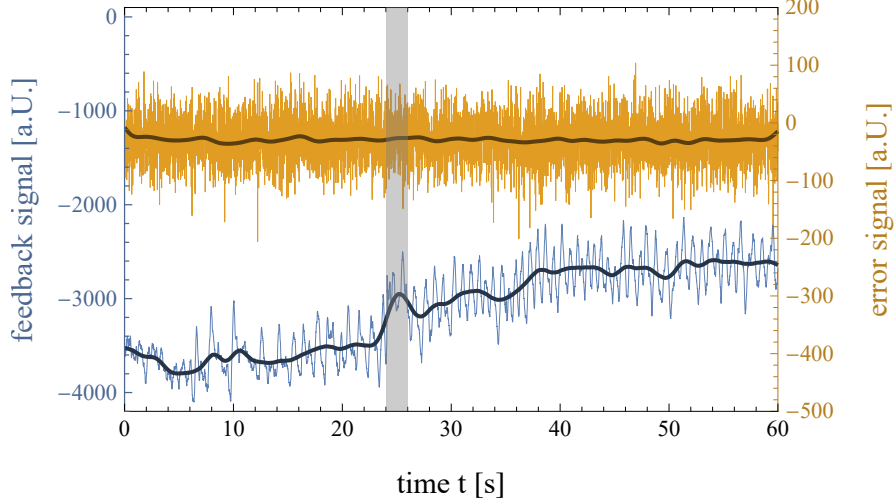


**Figure 14:** Feedback control signal (blue) and error signal (yellow) of the falling master laser on the mini drop tower. The gray bar marks the falling procedure time span.

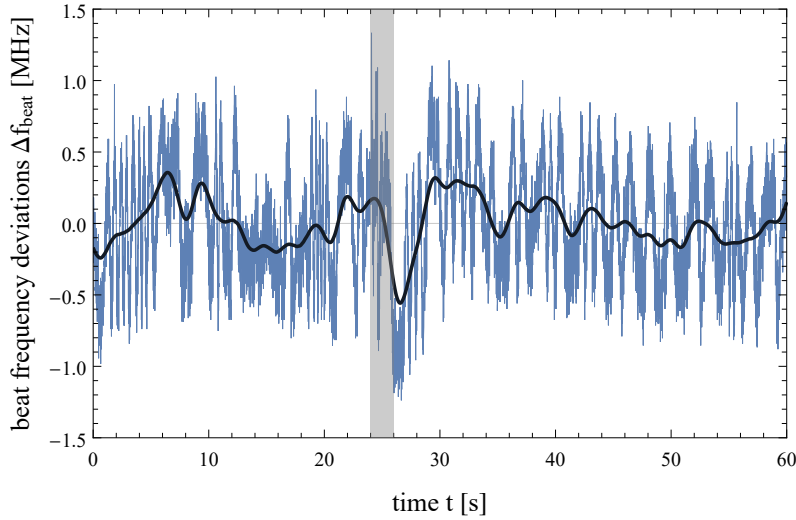


**Figure 15:** Beat note of the falling master laser and the stationary one on the mini drop tower. The gray bar marks the falling procedure time span.

### 3.3 Master laser autolock

Potential rocket missions employing atomic spectroscopy would require a certain automation in the experiment for compensating the limited bandwidth with the ground station[44][45]. As drop tower operations are easier and bandwidth is sufficiently available we can implement automatization test for exploration of such methods for future applications. One possible scenario is a set up of an automated frequency stabilization for the master lasers. This should take into account the two possible hyperfine structure transitions of potassium and the crossover ( $F = 2 \rightarrow F'$ ,  $F = 1/2 \rightarrow F'$ ,  $F = 1 \rightarrow F'$ ) [28] and allow potential locking on each of them. A possible set up in hardware was explored in the past[46] but for our experiment an implementation in software is necessary. To accomplish this we

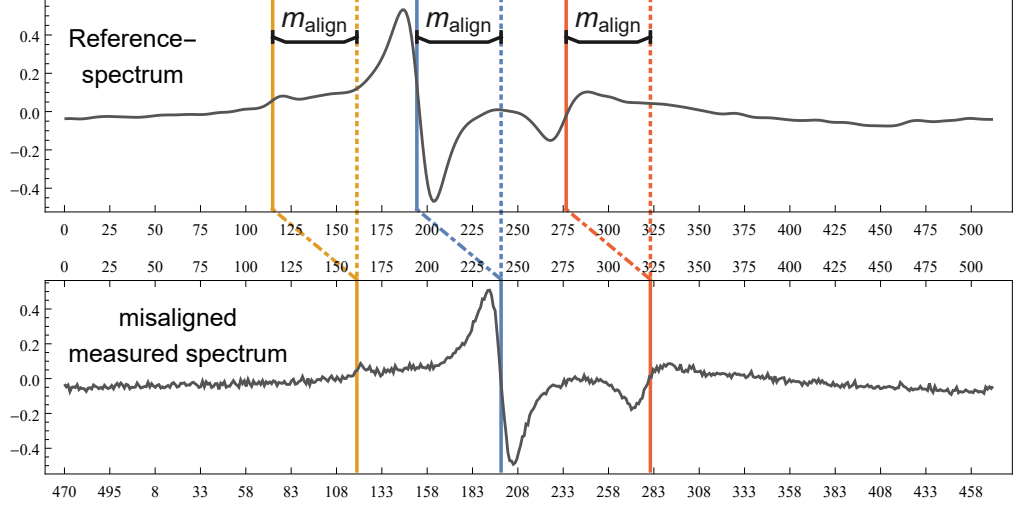


**Figure 16:** Illustration of the shift  $m_{align}$  of the measured spectrum (below) to the reference (above) and identification of the transition peaks. Both axes are in arbitrary units while the abscissa is proportional to a frequency and the ordinate to a power.

designed an algorithm which works by comparing the visible, measured spectrum by a prerecorded and filtered reference where the optical transitions are known. This yields a shift of the relative alignment  $m_{align}$  for the spectrums, as seen in [Fig. 16](#), and can therefore be used to power a feedback loop controller. This PID controller corrects the laser currents to match the spectrums according to the now known transitions and the predefined, desired lock point.

**Determination of  $m_{align}$**  To determine the alignment shift  $m_{align}$  we used various ways of calculating a correlation coefficient. This works with successive cyclic exchanges of the spectrums by one step and saving the coefficients to gather the maximum and minimum according to which algorithm is used (whether the maximum or minimum is used depends on the implemented algorithm). This specific point describes the shift at which the spectra agree the most with each other and are therefore congruent. We investigated four possible correlation formulas: a cross correlation [\[47\]](#), a derived cross covariance, a SAD (sum of absolute differences) and SSD (sum of squared differences) coefficient [\[48\]](#). A comparison is given in [Tab. 3](#) from the appendix. Finally we decided to utilize the cross covariance by default but keeping the other algorithms as an optional possibility. The correlation itself can be expressed in form of a mapping from the two spectra, denoted as two vectors with length  $N$ , to a sum

$$(\vec{x}_{ref} \star \vec{x}_{spec})(m) = \text{cov}_m^*(\vec{x}_{ref}, \vec{x}_{spec}) = \sum_{n=1}^N \begin{cases} x_{ref}^{(n+m)} \cdot x_{spec}^{(n)} & , n < N - m \\ x_{ref}^{(n)} \cdot x_{spec}^{(n+N-m+1)} & , n \geq N - m \end{cases} \quad (12)$$

where  $m$  is the applied cyclic exchange and  $\vec{x}_{spec}$  the mean corrected spectrum. The correction for the reference and measured vector is applied with

$$\vec{x}_{ref} := \vec{f}_{ref} - \bar{f}_{ref} \quad (13)$$

$$\vec{x}_{spec} := \vec{f}_{spec} - \bar{f}_{spec} \quad (14)$$

whereas  $\bar{f}_{\dots}$  denotes the mean of the respective vector elements and  $\vec{f}_{\dots}$  the original data while  $\vec{x}_{ref}$  is precomputed to save runtime. This adjustment serves two purposes: rectify shifts in the spectrum and ensure that most elements share the same sign which is necessary for the covariance to work. The alignment can finally be derived with

$$m_{align} = m_{trans} + \arg \max_m [(\vec{x}_{ref} \star \vec{x}_{spec})(m)] \quad (15)$$

Where  $m_{trans}$  is the position of the desired transition to lock on. One can already see that a rescaling adjustment is not required since the  $\arg \max$ -function is invariant under a multiplication of a positive constant (which justifies using just the covariance instead of the full correlation). The runtime scaling behavior can be seen by the fact that the correlation is defined by a sum which has  $\mathcal{O}(n)$  and the successive rotations which yields another  $\mathcal{O}(n)$ . Therefore the overall runtime scaling is  $\mathcal{O}(n^2)$ . Though for the modest number on points fetched from the TBus hardware (maximum 512 samples) the runtime is dominated by the hardware software transmit bandwidth which needs approximately 200 ms for gathering a whole spectrum while the alignment calculation runs for just about 180  $\mu$ s. This runtime was reached with implementing the time critical parts in c++ while using SIMD instruction sets for massive vectorization which then gets called by the LABVIEW program. To cut measurement time and increase the autolock frequency, an adaptive point acquisition, which changes the number of points requested from the hardware, was made. It was also noticed that the acquirement happens on a static grid which has to be taken into account. Therefore we only used sub components which represent sizes by powers of two (64, 128, 256, 512). This could possibly improved in the future by using linear combinations of various bases in the form  $\mathcal{B} = \text{span}(\{n \in [1; 9] \mid 2^n \leq 512\})$ . Furthermore to keep the calculations consistent we used a simple next neighbor interpolation. This still leads to a near continuous mapping because the reference spectrum gets to keep the full resolution despite the discontinuous measurement spectrum. To increase the automatization even further we also tested a visibility verification of the measurement spectrum which was solely based on calculating the standard statistical correlation [49] for the given  $m_{align}$ . This would enable future experiments to not only make the frequency stabilization setup but also start from zero laser current and find the spectrum position autonomously which is currently done per hand.

**Autolock algorithm** While a single alignment step would theoretically be sufficient to shift the spectrum to the right position (for TBus: index 256) there are multiple factors leading to the necessity of an iterative procedure. This includes the uncertainty in the laser currents, thermal deviations and a concurrent feedback loop of the temperature controllers. To compensate this, a PID controller was implemented. Hereby the parameter triple  $(P, T_i, T_d)$  defines the system transfer function

$$\Delta m' = D \cdot \left[ P \cdot m_{align} + \frac{1}{T_i} \int_{\tau} dt \cdot m_{align} + T_d \frac{dm_{align}}{dt} \right] \quad (16)$$

The additional fourth parameter  $D$ , called damping parameter, is introduced to make an easy and fast adjustment for the magnitude of the correction although this is not strictly needed since it is completely linearly dependent on all other parameters.

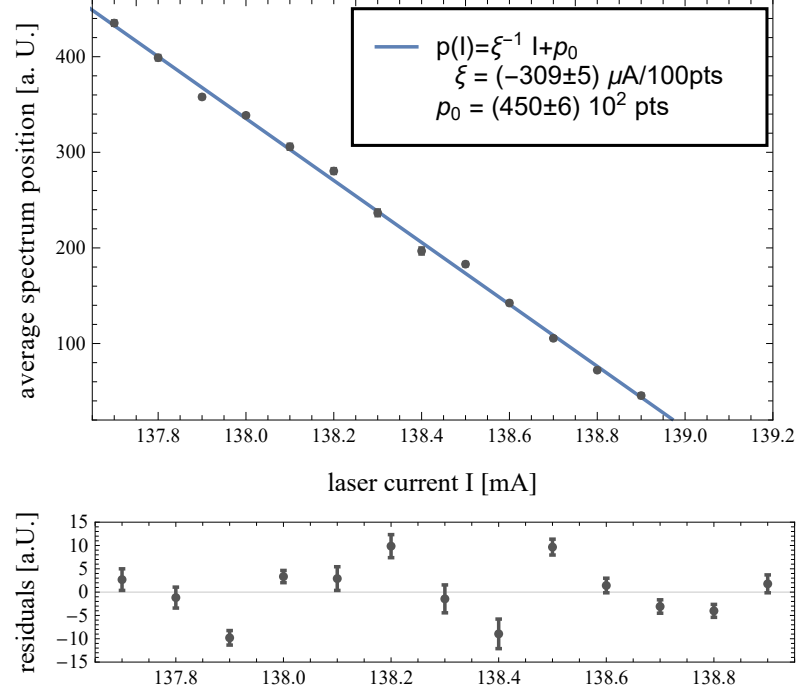


**Figure 17:** Average spectrum position in respect to the applied laser current. The data is fitted with equation (18) to acquire the  $\xi$  constant.

To convert  $\Delta m'$  to a usable current offset we assume a linear relationship which is scaled by a proportionality constant  $\xi$ . One can already see that a constant term is not needed here because a shift is not necessary when the spectrums are congruent (Although for the linear fit to determine  $\xi$  this is necessary since we measure the points in arbitrary units and offsets). Therefore we get

$$\Delta I = \xi \cdot \Delta m' \quad (17)$$

The parameter  $\xi$  was experimentally acquired with measuring the average of the crossover transition position by a specified current. It was found that

$$\xi = (-309 \pm 5) \mu\text{A}/100\text{pts}. \quad (18)$$

which can be seen in **Fig. 17**. This also provides a way of calculating the maximum control current to shift by the whole spectrum window. Assuming the lockpoint on the opposite side of the current point, which is therefore 512 pts. away, yields a control current of approximately  $I_{ctrl} = (1.582 \pm 0.026) \text{ mA}$ . While this solution is mathematically correct the assumptions above are the worst case in terms of distance of lockpoint to spectrum position. In reality the control current is about half the given value which takes into account that the lockpoint lays typically in the middle of the reference spectrum. This also enables the calculation of the maximum resolution and the conversion Factor of the TBus via measuring the distance in points of the optical transitions  $F = 1, 2 \rightarrow F'$  in **Fig. 4** and dividing this by the splitting frequency given in [28] ( $\approx 461.7 \text{ MHz}$ ). These two solutions can be combined to give the resolution per point (max. scanning amplitude) and conversion factor

$$\frac{\xi \cdot \delta m}{\Delta f_{F=1,2}} = \frac{\xi}{\delta f} = (1.070 \pm 0.018) \mu\text{A}/\text{MHz} \quad (19)$$

$$\delta f_{min} = (2.886 \pm 0.026) \text{ MHz} \quad (20)$$

Those factors can be used to build an extensive list of safety measures to prevent accidental damage due to failures in the calculations of the alignment. The most prominent example here would be the application of a valid current operation interval. This means, that the laser current  $I$  could only be altered in a given interval set by the starting current  $I_0$  and the control current  $I_{ctrl}$  as given with  $I_0 - I_{ctrl} \leq I \leq I_0 + I_{ctrl}$ . Currents above or below those thresholds get truncated and lead to an abortion of the autolock procedure to prevent any harm on the system. It has to be noted here that going out of this interval does not necessarily damage the system or does any harm. But it could certainly lead to an undefined/unclear state for the algorithm which could then yield big corrections due to noisy spectrums which in itself could trigger other safety mechanisms of the TBus or provoke corrections of the TECs which then can go into an error state. The core algorithm implemented and tested in the prebuilt BLASTEK capsule can be outlined in pseudocode and is shown in the appendix in Algorithm 1.

Although the program could directly employ the alignment calculation via the given formula (12) it is an extreme improvement of running time not to do the cyclic exchange (effective rotation) and instead do a convolution over a pre calculated array. This can be achieved by just repeating the reference spectrum a second time and treat the measured one as the convolution window function where outside points are vanishing. This can be precomputed and therefore does not include any additional overhead. This simplifies the formula to

$$(\vec{x}_{ref} \star \vec{x}_{spec})(m) = \sum_{n=1}^N x_{ref}^{(n+m)} \cdot x_{spec}^{(n)} \quad (21)$$

and improves the runtime over four times for the plain rotation and up to 20% to the derived formula (12) from above. This improvement comes mainly through better cache coherency, avoiding divisions and precomputing of data.

The fully implemented algorithm was thoroughly tested on the mini drop tower and was able to lock on all three transitions in a few seconds or less. Failure of the procedure were rare and often caused by bad PID parameters which were not optimized in course of this work. Therefore a full conclusion about the feedback state machine can not be drawn here. Nevertheless the algorithm worked really well for just setting slower Parameters in the Form  $\{K_p, T_I \ll 1, T_d \equiv 0\}$  so effectively implementing just a PI controller like KALEXUS did[44]. The adaptive sampling and interpolation for the cross correlation matching was also shown to work successfully and provide a good way to speed up future autolock procedures.

**Outlook and future developments** It was shown that the previously used autolock algorithms could also be applied to DFB diodes and work as expected. The improvements here can also be applied for future rocket and satellite missions. Especially the new implemented adaptive sampling method could significantly decrease the time to first lock and therefore speed up experiments.

A possible future and novel development could be a Monte Carlo probability based sampling method (ASAP: *Adaptive saturation probability sampling*). This idea consists of a probability distribution  $\mathcal{P}_t(m_{align}, t - \Delta t)$  depending on the last spectrum position which samples random, distinct points in the measurement spectrum. This is done with incremental correlation and alignment calculations[50] until a correlation threshold is reached (i.e.  $p > 1\sigma$ ). Then the alignment pass is considered done

and the spectrum position defined. This could dramatically decrease the number of sampling points needed for each alignment step. An application of this idea is especially important where calculation time as well as data acquirement times are scarce. A situation where those criteria are fulfilled are satellite missions. Such ventures are already proposed or in their design study [51–53] and could strongly benefit from this.

### 3.4 Evolutionary swarm optimizing of TECs

The optimization of PID controller is often done by semi empirical procedures. An example of those are the Ziegler-Nichols method[54] or the more sophisticated Cohen-Coon approximation[55]. Both of which rely on a kind of reaction curve formed by known parameter sets where certain features are extracted from. These features can be used to calculate a shift for the used parameters. This then gets refined multiple times in an iterative approach until an adequate set is found for the given task. A failure of those methods is rare and often caused by too optimistic assumptions or other hidden reasons. In those cases the PID controller has to be optimized by hand to either find a better starting point for the automatic methods or to obtain an already sufficient parameter triple.

The manufacturer of the TEC controller provided an *auto tuning algorithm* with similar working techniques to the methods described above. While this tuning worked great for the MOPA lasers, it produced nonoptimal controlling values for the master lasers. Traditional methods of mathematical root finding procedures like the Newton method or gradient descent can not be used. The cause of this lays in the intrinsic property of those systems to have a semi deterministic and noisy behavior. This makes it next to impossible to create a stable Jacobian matrix and to get enough momentum to overcome local minima. Therefore an applicable optimization must be derivative free and relative insensitive to noise.

To obtain good parameter values, an algorithm based on evolutionary principles was created. Those algorithms are already, in similar fashions, in use in different experiments to optimize atom numbers in magneto-optical traps[56, 57]. An additional advantage of this method is that it can handle a parameter space  $\mathbb{P}^N$  with a great number of dimensions  $N$ . Although for the PID controller  $N = 3$  is relatively small, it was shown that this is still an appropriate procedure[58] for a wide range of applications.

In the specific case of a TEC controller, an algorithm based on particle swarm optimization[59], evolutionary strategies[60] and principles from Ref. [56] was implemented.

**Algorithm structure** The algorithm works by utilizing the main three evolutionary strategies[60]

1. Recombination: Two individuals share and combine their genetic material to produce a new entity.
2. Mutation: The genetic material of one individual gets altered.
3. Selection: The strongest individuals survive by adapting faster to their changing environment while the weaker counterparts die with their respective genetic material.



It starts by a single, provided parameter set. With multiple mutations in all Parameters  $N$ , an initial generation with  $n_{init}$  individuals is created.  $n_{init}$  is hereby the first hyper parameter which has to be chosen beforehand. The recombination is skipped in the first iteration and all species getting a fitness value assigned. This value ranks them in their ability to control the temperature of the laser. The assignment is done via a fitness function which is explained in detail later on. Then the selection stage begins and only the best  $m$  individuals *surviving* for the next generation. The other  $N_{init} - m$  individuals are considered *extinct* and getting deleted. After this the algorithm goes into an iterative procedure of evolution. Here every generation begins with  $q$  mutations of one or more parameters, recombination of maximum  $r$  individuals were only non mutated ones are considered and a selection stage where each new or changed species gets evaluated with the fitness function and deleted if not under the best  $m$  performing individuals. A rough pseudocode implementation is given in Algorithm (2) in the appendix.

Recombination was implemented with a randomly chosen 50:50 share of the genes from the parents to their offspring. The mutation was handled by introducing three hyper parameters which represent a standard deviation of the average amplitude of change. A Box-Muller transform[61] then created a random shift for the parameter which gets applied to the new species. In ten percent of all mutations two parameters were altered, while in one percent all three were changed.

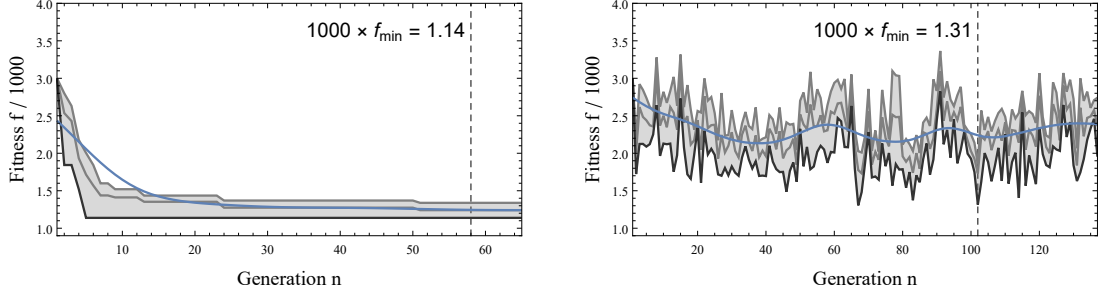
**Experimental reevaluation** To prevent an over dominating species due to coincidentally favorable circumstances while evaluation, an experimental reevaluation was introduced. This affects every individual which survived more than  $h$  generations. Those individuals get a reassessment of their fitness value. While this prevented an overly optimistic optimization as seen in *Fig. 18a* it also introduced artificial throwbacks in the general fitness. Choosing a constant reevaluation with  $h = 1$  like in *Fig. 18b* also hurts the process since it introduced too much new coincidentally good or bad sets. This leads to noise which prevents the overall process from converging. Typical applied values were in the regime of  $h \approx 10^1$ .

**Fitness function** Deriving a fitness function for an evolutionary algorithm can be a delicate subject when no objective measure of performance is available. In the upper mentioned publications, the atom number was a good indicator for this value. For the controlling performance of PID parameters on the other hand, no obvious or universal value is known. To create a good measure, one has to take all necessary boundary conditions into account. For this purpose four conditions could be phrased:

1. Fast reactions to compensate deviations in the control variable
2. Minimal deviations around the target point
3. Short and long term stability
4. Suppressing of periodicity in the control signals

To ensure all conditions a fitness measurement procedure was derived. One evaluation pass begins with setting the new parameter set by a temperature of  $T_1$ . Followed





(a) Evolutionary TEC optimization without experimental reevaluation over 65 generations.

(b) Evolutionary TEC optimization with continually experimental reevaluation over 130 generations.

**Figure 18:** TEC fitness evolution with no reevaluation ( $h = \infty$ ) and with continually reevaluation ( $h = 1$ ). It has to be noted that the right figure is double the time span from the first. The black line denotes the current best value, the surrounding gray area the minimal and maximal span. The line in the middle represents the current mean whereas the blue colored line is the lowpassfilter trend of all parameters.

by a four second pause which allows the new values to settle and stabilize the laser. Then the first measurement section started where a number of points was captured. Immediately after this, the target temperature was set to  $T_2 = T_1 + \Delta T$  followed by a one second pause to provide a short settle period. Then another measurement interval is started which captures as many points as the first one. A defined fitness function layed out in equation (22) then maps the two data sets to a single fitness value  $f_{fitness}$ .

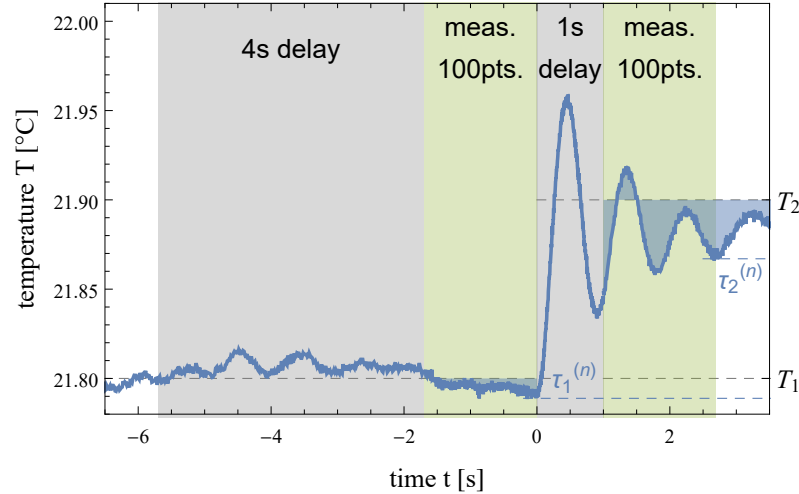


**Figure 19:** Numerical simulation (see equation (30) in the appendix) of a pass to calculate the fitness function of a Meerstetter TEC. In Order: Set Parameter; wait for four seconds; measure 100 samples; set nominal-temperature to  $T_2$ ; wait for one second; measure another 100 samples; calculate fitness function according to equation (22)

The procedure can be reasoned according to the different conditions aimed for. The first pause followed by the measurement ensures a long term stability, minimal

deviations around the target temperature and a suppressing of periodicity. The jump in temperature, with the delayed second measurement tests the short term stability, fast reaction to deviations and also the damping of periodical controlling.

$$f_{fitness} : \mathbb{R}^n \times \mathbb{R}^n \rightarrow \mathbb{R}^+ \mid \vec{\tau}_1 \times \vec{\tau}_2 \mapsto \begin{cases} \infty & ; \quad |\tau_1^{(n)} - T_1| > T_{crit.} \vee \\ & ; \quad |\tau_2^{(n)} - T_2| > T_{crit.} \\ \text{std}_{T_1}(\vec{\tau}_1) + \text{std}_{T_2}(\vec{\tau}_2) & ; \text{sonst} \end{cases} \quad (22)$$

The mapping function is in principle only the standard deviation of both measurement intervals with two details. The fitness is considered inadequate when the absolute distance of the respective target temperature and last data point is exceeded by a critical value  $T_{crit.}$ . This is evaluated to an effective infinite fitness. Also the standard deviation is not mean corrected as by default but bound to the target temperature as defined in (23).

$$\text{std}_T(\vec{\tau}) = \sqrt{\frac{1}{n-1} \sum_{i=1}^n (\tau^{(i)} - T)^2} \quad (23)$$

This ensures that the evolution will not produce slow, minimal parameter which have a slow deviation around their mean while fulfilling the distance requirement. The arising fitness value also has an approximate interpretation of an average of half the RMS around the target temperature after a change of  $\Delta T$  additional to the background RMS deviations.

**Measurements and results** Multiple preliminary tests and five full measurements were conducted to optimize the TEC parameter. The full experiments were made overnight in a time span of more than 10 hours. This required some automated safety measures to protect the lasers as well as the TEC chips.

The experimental setup features one of the master lasers interfaced through the TBus to the LABVIEW control program. This provides the default laser controlling scheme. For the experiments a constant current in scanning mode was set. This value was chosen, so that the potassium spectrum is visible to mimic the real use conditions. The TECs were connected directly to the computer via USB and another digital GPIO channel was interfaced to a readable DAQ card. While the USB connection was used by the optimization program, the digital channel was read out by the LABVIEW control program. This distinction was made since it was not possible to establish an information exchange from the VI of the PXI to the evolutionary program on the control laptop. But both programs need to know the TEC state to prevent laser damage when a bad parameter set brings the temperature controller into an error state. The digital channel accomplished this by implementing the setting that the meerstetter sends a digital signal whenever it goes into an error state while the C-sharp program can read this out directly through the USB interface. Although this feature was thoroughly tested, it was never needed in the overnight measurements.

Some important, typical hyper parameter intervals tested were

- Initial population size:  $N_{init.} = [50, 100]$

- Population count:  $m = [5, 15]$
- Mutations per generation:  $q = [3, 10]$
- Recombinations per generation:  $r = [3, 10]$
- Reevaluation count:  $h = [5, 30]$
- Temperature difference:  $\Delta T = 0.1 \text{ K}$

The starting parameters were chosen from the experimentally determined sets of the mini drop tower tests. Upper and lower bound were always readjusted and often made big enough to not interfere with the optimization. The standard deviations for mutations were also started with significant large values. After some fitness-unchanged generations, defined with  $k = 15$  as a new hyper parameter, the standard deviations were halved to aid converging to a minimum point. This helps to minimize momentum in the parameter variations. The momentum is beneficial in the start to overcome local minimums but is undesirable later on.

The best optimization recorded reached a fitness of  $1000 \times f_{fitness} \approx 0.96$  with the time evolution displayed in [Fig. 20a](#). The parameter development can be seen in [Fig. 20b](#). It is clearly visible that the best fitness was reached in a minimum of deviation in the PID triple. This then was disturbed by a reevaluation kick one generation later. However, afterwards it turned out to be the optimum rather than a local minimum. The resulting parameter set was then implemented in the master laser TEC control and later used in the Bremen drop tower.

To estimate the improvement of the new PID triple, a test was conducted which just captured the reaction curve by a temperature change of the used  $\Delta T$ . It was run with the old and new parameters respectively to allow a simple comparison. This can be seen in [Fig. 21](#). It is clearly visible that the new set provides a nearly aperiodic behavior after one oscillation period whereas the old parameter goes into a slow dampened oscillation. Also the reaction peak is much smaller and deviations before and after can be seen to be under better control.

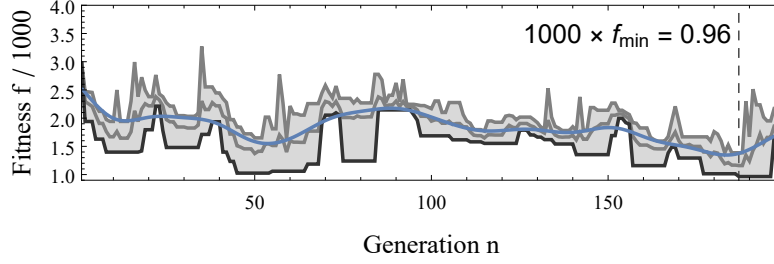
This shows that the evolutionary algorithm was effective and improved the temperature stabilization as desired.

**Future outlook** To improve the results, a new fitness function which takes the local slope into account to make the aperiodic curve fall faster could be derived. This can lead to a faster settling on the target temperature and therefore the ability to counteract sudden deviations.

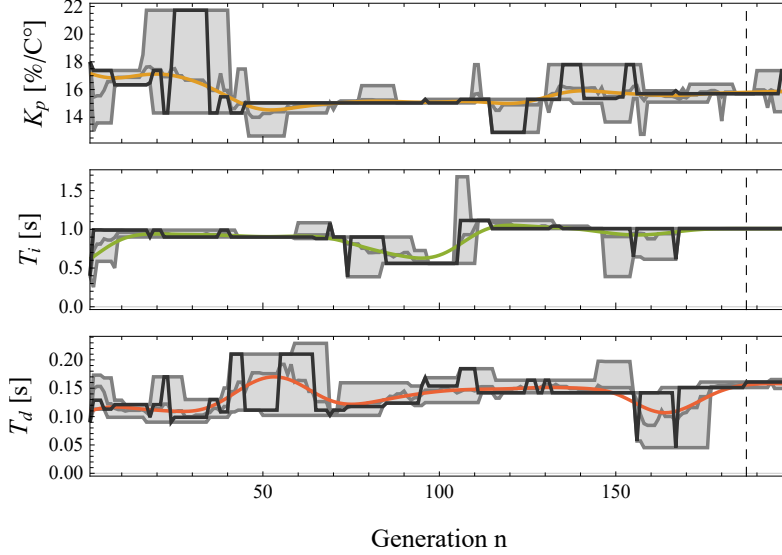
Measuring 10 hours is a long time for optimization procedure. As mentioned in [Ref. \[56\]](#) and described in [Ref. \[57\]](#) a differential evolution approach[\[62\]](#) can aid the process. This exploits the fact that normal evolutionary algorithms tend to locally converge in a near constant direction. We can therefore predict the change for future generations. For a parameter  $p_i$  of an individual  $j$  in generation  $N$  we can therefore write

$$p_i^{(j', N+1)} = p_i^{(j, N)} + F \cdot \delta p_i^{(j)} \quad (24)$$

where  $\delta p_i^{(j)} = p_i^{(j, N)} - p_i^{(j, N-1)}$  is the difference of the parameters from the last generation and  $0 < |F| \leq 1$  is a real number. The sign of  $F$  is positive if the fitness



(a) Evolutionary TEC optimization of fitness value. An over threefold improvement can be seen.



(b) Evolutionary TEC optimization of the parameter PID triple.

**Figure 20:** A 199 generations long evolutionary optimization with a moderate value of  $h = 10$  for reevaluation kicks. The fitness value (blue) can be seen to improve by a factor of three to the starting value. The three parameters ( $K_p$  yellow,  $T_i$  green,  $T_d$  red) can be seen to converge well for the best fitness in generation 187. A majority of the fitness improvement (approximately half) was made in the initial generation with a starting population of  $N_{init.} = 100$ .

increased from the step before and negative for the opposite case. The magnitude of  $|F|$  is called amplification constant and can be chosen as a hyper parameter. Another possible implementation is an adaption of the steepest descent linear optimization technique[63]. It applies a species wide shift and is therefore denoted with

$$\delta k_i = \frac{\sum_j \delta p_i^{(j)}}{\sum_j \delta |p_i|} \quad (25)$$

Another possible improvement could be made by trying other derivative free algorithms like the interval-geometry based Nelder-Mead method[64] with a improved restart procedure described in Ref. [65]. This method basically is an algorithm which holds a spanning interval of each parameter dimension and reduces and shifts those boundaries to converge to the deepest minimum. This could possibly converge faster than the evolutionary algorithms but is probably not that noise resistant. So both algorithms could be used were the Nelder-Mead method decreases the search

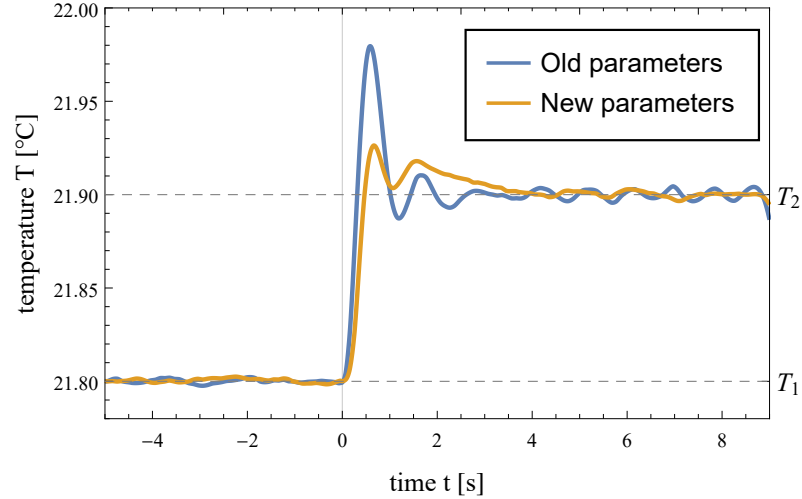


**Figure 21:** Result of an evolutionary optimizing after approximately 100 generations. The new parameters exhibit the more desired behavior in its nearly aperiodic reaction to a temperature change of  $0.1\text{ }^{\circ}\text{C}$  while the old parameters went into a slow dampened oscillation.

space in a rapid fashion where afterwards the evolutionary algorithm with differential evolution convergences with a great accuracy to the global minimum.

### 3.5 Qualification results and conclusions

It was successfully shown that the TECs and master laser can withstand and function after being exposed to strong accelerations. With over 90 test drops at the mini drop tower, this ensured their working capabilities for the Bremen drop tower and enabled the preparation for this as a next qualification stage. Also, the nominal working conditions of the capsule systems already present were verified.

Multiple problems especially with the RF electronics were compiled and either remedied or noted for later investigations.

Also the relative short and long term stability of the master laser beat note was shown which gave a good indication of the stability of a single laser in drop tower operations with the best performance at around 16s integration time. Multiple influences on the signals were observed and prevented in the final capsule. This especially concerns ground loops and cross talk between the cables.

A primitive and later improved autolock algorithm was shown to work with DFB diodes and provided a good future ground test bed for upcoming developments and applications. The temperature stabilization of the master laser was also significantly improved by a novel evolutionary algorithm for the temperature PID controlling. This will provide far better resistance to deviations in the drop tower operation.

In conclusion, the mini drop tower gave a first qualification test for multiple parts of the capsule systems, enabled significant progress for the capsule build and provided a preliminary preparation of the setup for Bremen.

## 4 Qualification stage II: Bremen drop tower

The Bremen drop tower is a scientific facility, operated by ZARM FABmbH, to provide experiments a micro- $g$  environment. It is a 146 m high tower with an outer concrete hull and an inner 120 m high steel tube. A schematic can be seen in [Fig. 22](#). Within the inner steel tube, vacuum down to below 0.1 hPa can be created. Special, pressurized, battery powered capsules designed for the drop tower are used for drop (and catapult) experiments. While falling, the capsule experiences near

weightlessness. This can be used as an alternative or stepping stone for rocket or satellite missions. Those mission costs are often in the millions while a drop tower test is only a tiny fraction compared to that. It is also a lot easier, the system can be made much more accessible and multiple drops per day are possible.

Therefore the final qualification stage, before integration into the QUANTUS-2 experiment, is testing the laser system inside the tower. The capsule can be operated in two modes. A drop mode where the experiment is pulled to the top and then dropped for a micro- $g$  time of approximately  $t_{drop} \approx 4.7$  s and the catapult mode where the capsule is shot up from the bottom, effectively doubling the free fall time to  $t_{catap.} \approx 9.3$  s. Since the QUANTUS-2 experiment is able to operate in both modes, the qualification will happen with the catapult. This is reasoned in the stronger forces occurring while being shot up [\[67\]](#). Typical forces with the local acceleration of gravity  $g_0$  are given with about  $30 g_0$  for 280 ms in the catapult shot. For the deceleration while recapturing these values can vary from  $25 g_0$  for 200 ms up to  $50 g_0$  in just over 11 ms. The stopping force on ground is caused by a bath of polystyrene pellets. Therefore it is nearly constant and independent from the capsule. The stopping time is thus

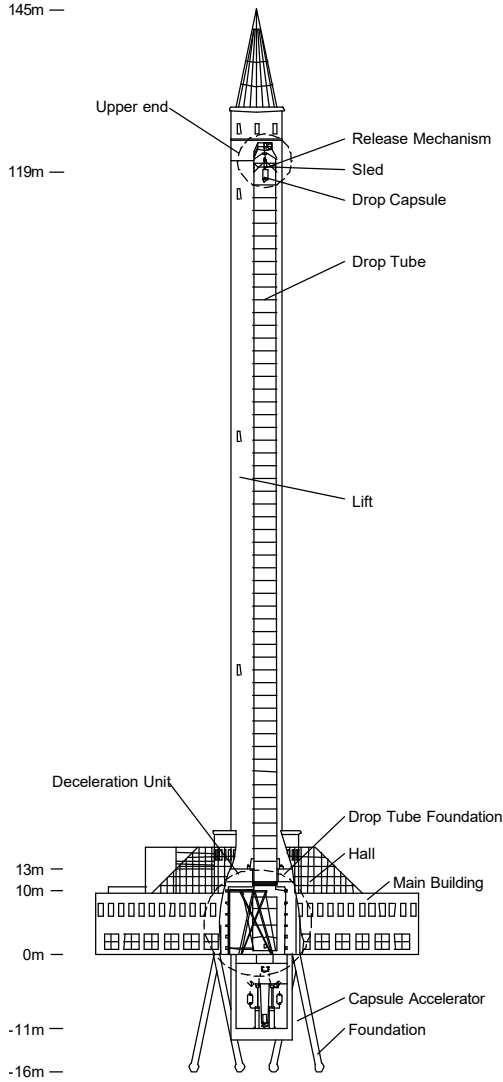


**Figure 22:** Schematic of the Bremen drop tower. Image taken from [\[66\]](#).

inversely proportional to the weight. Typical accelerations of a catapult start from the BLASTEK experiment can be seen in [Fig. 24](#). The micro- $g$  time forces can be kept to a residual acceleration of about  $10^{-6} g_0$ . This value is reached by creating a vacuum in the inner tube with a quality of  $< 0.1$  hPa. The depressurizing phase takes about two hours. Another 15 minutes is needed were the piston gets

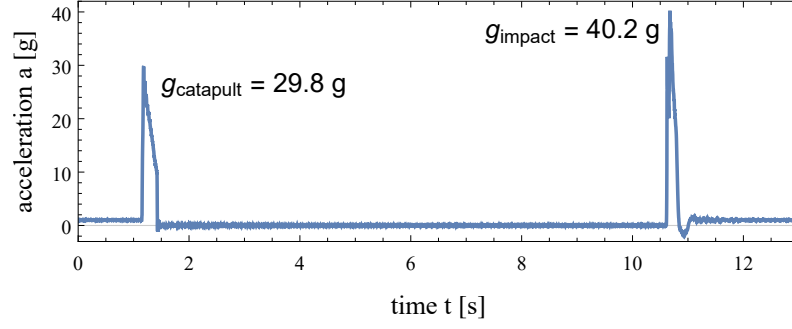


**Figure 24:** Acceleration of z component in a catapult start and impact. The linear decrease in catapult acceleration as well as the two impact peaks due to the capsule geometry are visible.

lowered 11 m down and the catapult is pressurized for the shot. This also requires a separation of the umbilical cables and the capsule which is from then on self-sufficient. The controlling is ensured via a Wi-Fi connection in the inner tube and thus connected to the control laptop. After everything is prepared the measurement sequence is started and the catapult start is initiated. The PXI captures the experiment relevant data while the ZARM computers monitor environmental parameters, in particular accelerations and rotations. While the capsule is falling, the deceleration container at the tower bottom is moved to a position above the catapult in order to capture the capsule. After the impact, the tower is pressurized and the experiment is retrieved.

**Catapult capsule** The Bremen drop tower differentiates between three different capsules. They all differ in size and task. Only one of those models is able to be used in the catapult mode. The schematic of this is shown in *Fig. 23*. In this figure six distinct areas can be identified. In order:

1. The tip of the capsule is the last thing mounted before deployment. It consists of a small front area of about  $6\text{ cm}^2$  where the capsule stands on in the catapult. This is followed by a tapering cone and the last few centimeters by a sharper cone segment. This design has a side effect of producing two different deceleration peaks. This can easily be seen in *Fig. 34b* in the appendix.
2. The batteries section which supplies the capsule power in self-sufficient mode.
3. The ZARM computer layer provides the computer for controlling the capsule systems and data capturing.

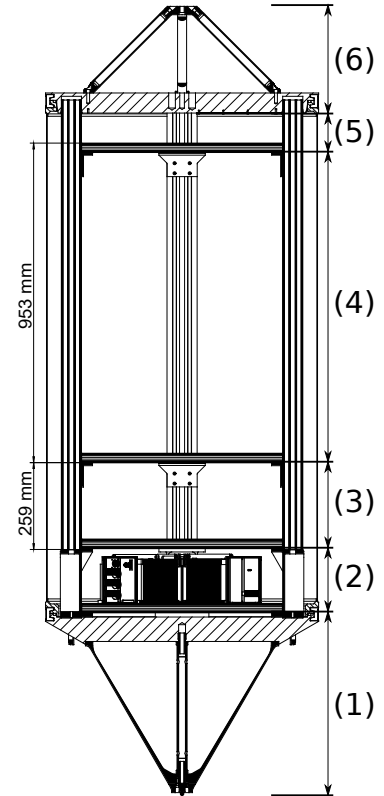


**Figure 23:** Schematic of the small, catapult capsule. Image taken from [67].

4. The payload layer can be subdivided by sublevels and is the fully provided volume for the experiment.
5. The last volume layer is used for calibration purposes of the center of mass and as a place for the wireless transceiver.
6. The upper holding arms are used to attach the capsule to the tower winch.

As specified, the whole experimental apparatus has to fit into the payload layer which can be further subdivided into smaller levels. For the whole BLASTTEK capsule, this meant to pack in the whole laser system, laser electronics, the control computers, telemetry and the power supplies. A photo of the BLASTTEK structure can be seen in *Fig. 2a*. The topmost level was chosen to locate the laser system. It also carries the master laser and the fiber coupled photodiodes. The second stage houses the most controlling electronics like the TBus stack, temperature controllers and the transimpedance amplifier. This was followed by a second electronics stage with the DAQ card and the RF electronics. In the last level, the PXI, DC-DC converter and additional batteries for the system were included.

This structure was held and reinforced by four stringers on which the platforms were mounted. The capsule hull was then fastened around it and the nose cone installed. A photo of the full operational capsule can be seen in *Fig. 2b*.

## 4.1 Data capturing

Capturing the data in the catapult sequence over a period of tens of seconds is an extensive task. The monitoring has to record up to 150 distinct data streams from six different subsystems. Four of them are handled by the TBus stack. This requires a versatile capturing sequence to allow for different measurement directives. To reach this, the procedure was included in the general control program. This then acts as a state system for the measurements thus allowing changes in the experiment without any hard coding. This is realized with the exception of the frequency card because a data capturing without the FIFO mode is not useful. The starting state of the card is then restored after the sequence to allow for a uninterrupted experimental control.

Three different running conditions were implemented. A sequence with a freely selectable time span, one with a selectable data cap and an interminable mode which needs a user action to be ended. For Bremen drop tower sequences the time bound mode was always chosen with a duration of 30 s. With all streams enabled the program reached a capture rate of about 6 Hz. This was severely limited by the TEC measurement and big data chunks from the TBus power supplies. Later starts with just the frequency controller and photodiodes reached up to 40 Hz with over 1100 samples. This allowed to resolve events in those streams with an accuracy of 25 ms.

The program allowed a rough, arbitrary selection of which streams to record. This included

1. Power supply (TBus) - The two power supply cards (ADC) of both TBus stack halves allowed for capturing all provided currents, voltages and temperature of the converters. For both cards this meant a bulk of 64 data points for every time step.



2. Laser controller (TBus) - The laser controller cards could transmit their current values and temperatures of the output stages.
3. NTC sensors (TBus) - All connected NTCs could have their resistance read out. The channels had to be hard coded into the program.
4. Frequency controller (TBus) - The frequency controller card reported back various signals for the laser stabilization. Seven values (of all 16 FIFO channels) were of particular importance. The three offset lock frequencies and the feedback loop control signals of all MOPA laser and the master laser, respectively. Two different modes were implemented. One with a direct continuous dumping and a snapshot mode. This is explained in detail later on.
5. Optical power - The amplified and converted voltage from the transimpedance amplifier card of all configured photodiodes. The configuration was also hard coded.
6. Temperature controller through the MeCom XPort - The temperature of the Meerstetter TEC controller and their current. The current and temperature could be toggled separately from each other.

The recording sequence took place entirely in the main memory of the PXI. This prevented capture rate degradation due to limited IO throughput. A 30 second sequence produced about a megabyte of data so this was not a constraint for the computer. Final hard drive saving happened immediately after the sequence and took less than a second.

Except from the ADC scaling, some captured values were not computed to their final result and had to be calculated in the evaluation process. This not only reduced the program complexity but also saved time and therefore capture rate. This required a conversion of some values at the evaluation which was realized in an automated MATLAB script. For all streams except the frequency card, this could be implemented as a raw data dump with a static size  $n \times m$ .  $n$  hereby denotes the number of time steps made and  $m$  the number of channels of the respective stream. The FIFO data on the other hand was not able to be fitted inside a statically sized grid since the buffer size of each time step could vary. Also a single time step could mean multiple repetitions of the 16 channels or even less than all channels. It can be concluded that the single time step system used for the other streams can not be applied here. As a solution to this a data structure protocol was conceived. It exploited the property of the FIFO stream to only encode all values as unsigned and therefore positive integers. This allowed for injecting the time stamps after each buffer read out between the data stream. The time stamps were increased by one and negated to differentiate them from the real data values. Thus the output is a continuous array of values with encoded time stamps in between. In the evaluation process these stamps were extracted and encoded. The exact timings for every point was then linearly interpolated from the next neighbor time values. This assumption is valid since the frequency controller card updates the FIFO buffer in constant time intervals. The protocol allows therefore an asynchronous time capturing with a static time stamp method.

For enabling future long time measurements a FIFO snapshot mode was tested. This used only a single 16 value window in the whole buffer. This eliminated the need

of asynchronous time interpolation, offset detection and incorporated the frequency card in the static  $n \times m$  dump. Although this seems like a huge benefit, it decreases the amount of refreshed data from the card and can thus only be used in long time measurements where a high resolution and data rate is not needed.

**Data evaluation prerequisites** After the drop, the data is retrieved from the PXI and evaluated as part of the post-analysis. Following three notes can be made about the evaluation of the data:

1. All temperature values measured are in voltage values. To convert this, a voltage-resistance-temperature approximation must be made. The voltage-resistance conversion is calculated with the standard Ohm law. The resistance-temperature approximation relies on two temperature points where one reference value is known. In the experiment 10 k NTCs were used. This means that at  $T_0 = 25^\circ\text{C}$  the resistance is at exactly  $R_{T_0} = 10\text{ k}\Omega$ . For the temperature approximation we used the  $\beta$ -parameter equation[68]. The third order correction was neglected because the leading first order is already sufficient in its standard relative error[69]. The equation can thus be written as

$$T = \left( \frac{1}{T_0} + \frac{1}{\beta} \log \left[ \frac{R_T}{R_{T_0}} \right] \right)^{-1} \quad (26)$$

where  $\beta = 3650\text{ K}$  is a given material constant.

2. Using the FIFO mode has a serious disadvantage. It is not known where the buffer index starts since the frequency card cannot convey this information. So the capturing is started in an arbitrary position within the 16 channels. To be able to assign the channels an automated offset detection was made. It uses the fact that the last four channels from the frequency controller are not used and are therefore zero. With the index of the first zero from the block being  $i$  the offset  $o_{fifo}$  can be calculated by

$$o_{fifo} \equiv i + 4 \pmod{16} \quad (27)$$

3. Due to still unknown problems, the MeCom XPort sends invalid answers in about half the requests. The first few bytes seem to be always affected by a corruption. Luckily, the data payload is located at byte eight in the answer package. It was observed that high bytes with low bytes in the beginning tend to damp the faulty behavior even faster which can be steered with setting a prepared transaction number. Thus despite corrupted bytes in the beginning the data can be extracted every time. Nevertheless this falls to burden for the CRC16 checksum which can not be checked in those cases. Still, until today no corrupted temperature or current was ever obtained in one of the sequences. Although the data receiving could be corrected another error is known and not resolved to date. In the Bremen drop tower the XPort was observed to sometimes lose connection to the PXI at the catapult start or impact. This does not affect the TEC performance but eliminates the ability to monitor their temperature. It also crushes the data capturing rates because every TCP request results in a set 0.1 s timeout. A reconnect seems to help only for some seconds but is also subsequently dropped. This hints to a faulty XPort but is unconfirmed to this date.

## 4.2 Drop tests and sequences

To allow for proper preliminary judgement of the system, multiple drop simulations were conducted. This served mainly the purpose to assess how the different sub-systems would react under hour long self-sufficient operation, temperature changes, laser lock ability and battery performance. To have the simulations as realistic as possible, the capsule structure was wrapped in bubble wrap. This helped isolating the inside from the laboratory. All conducted tests were successful with the last simulation being nearly two hours long. It also helped to devise the used sequence strategy, layed out above.

### 4.2.1 Drop procedure

Every drop procedure begins with preliminary measurements in the laboratory to confirm that everything is working nominally. These sequences are already conducted on self-sufficiency with the whole power being supplied by the capsule batteries. The only umbilical connected to the capsule in those moments is the ethernet data cable.

After confirmation that the system works normally, the capsule is handed over to the drop tower team. They are mounting the hull and hermetically seal it so that the inside stays pressurized. After assembling, the capsule is hung onto the wench in the tower. There the nose cone gets added and the whole apparatus is placed on the catapult piston and connected to the umbilical. Afterward the inner drop tube gets sealed and a two hour long depressurizing phase begins. Hereby, the inner air gets thinned down to less than 0.1 hPa. Before and while this happens, first measurement sequences in the tower are conducted. This serves the purpose of checking the system status and acquiring comparison values for the flight and afterwards. Around 15 minutes before the inner tube is fully evacuated, the catapult gets loaded. This is done via disconnecting the umbilical to the capsule and lowering it down. Meanwhile the catapult hydraulic start system is building up pressure. No sequences can be conducted here, because the wireless connection often drops out in this time span.

When the tube is evacuated, the capsule is positioned and the catapult is pressurized, the system is ready to launch, waiting for confirmation from the FAB team and the experimenters. Seconds before confirming the shot, the measurement sequences are started and run in full speed for a predefined time interval. This spans the whole start and impact time and was chosen to be 30 seconds. For typical flights an start acceleration of 30 g, a flight time of 9.2 s and an impact deceleration of 41 g were registered. Since the capsule was not changed significantly over all flights made so far, these values were nearly constant.

After impact and finishing of the sequence, the inner tube is being pressurized again. Subsequently the last measurement is done. This is made to assess the aftermath of the deceleration forces. Thirty minutes later the tube can be opened again and the capsule can be recovered out of the polystyrene bath. The following demount of the hull marks the end and the capsule is handed back and towed into the laboratory. The data files are being downloaded already in the tower and after every sequence through the wireless connection.

### 4.2.2 Conducted drops

Until finishing of this thesis, BLASTEK made six flights from a catapult start in the Bremen drop tower. The first three drops were the initial test drops. The third one was the first to reach a full speed continuous measurement. Following starts were conducted to further investigate the optical powers in the system. In order with more detail:

1. **Catapult start 1 - 18.01.2018** First drop for initial system test.  
Proof of concept confirmed and full system capabilities were shown. Unfortunately the MeCom connection dropped on impact. Thus the data rate of everything except the asynchronous frequency card was decreased significantly. Because of safety reasons, the measurement after impact was omitted since the TEC states were unclear.
2. **Catapult start 2 - 19.01.2018** Confirmation for the results of the first drop. Also a new disconnect circumvention for the TEC was tried but failed to work. The TECs dropped the connection on catapult start. This lead to a weak data coverage of the flight. Nevertheless a whole program restart and reestablishing the MeCom connections lead to a successfully measurement in the deceleration chamber.
3. **Catapult start 3 - 19.01.2018** Result validation flight. All systems kept in connection and a whole data set was acquired. Deviations in the output and intermediate light powers in the system was noted.
4. **Catapult start 4 - 12.02.2018** First try of fixing the observed deviations in the optical output power. From now on the NTC, ADC and TEC currents are not captured any more to increase the data rate.
5. **Catapult start 5 - 22.02.2018** New installation of some photodiodes on other places and test of the power deviations issue. Partial success could be reached on less noisy optical power signals. For this investigation only the frequency card and the PD signals were monitored.
6. **Catapult start 6 - 28.02.2018** Further coupling and beam walking through the system paired with stronger fastening of the optical elements lead to no significant improvement compared to flight five. Hints of an electronics issue causing the fluctuations are found.

General data like accelerations, time of flight and rotations for every drop are given in the following table

**Table 1:** General values for every conducted Bremen drop tower catapult flight.

Nr.	Start acc.	Impact acc.	Flight time	$z$ -Rot.	$x$ - $y$ tilt	Laser lock	TEC
1	30.1 g	41.6 g	9.20 s	9.34°	3.04°	✓	×
2	29.8 g	40.2 g	9.18 s	9.94°	2.22°	✓	×
3	29.8 g	41.5 g	9.14 s	8.91°	4.13°	✓	✓
4	30.3 g	42.0 g	9.19 s	9.07°	3.33°	✓	×
5	29.9 g	41.5 g	9.22 s	9.54°	3.80°	✓	-
6	29.6 g	41.0 g	9.17 s	9.97°	2.38°	✓	-

### 4.2.3 Data evaluation

**Temperatures** Temperatures can be measured out of four different sources: capsule NTC sensors, capsule sensors employed by the ZARM, TBus card sensors and the laser temperature controller.

For a full two and a half hours long catapult sequence, the experiment is subjected to a steady temperature rise due to the electronics running the whole time. This also leads to a temperature gradient. On average the temperature increases by around 3.1 K. The biggest change happens on the second electronics platform, where the RF components and DC-DC converter generates most of the heat which leads to an increase of +4.7 K. The most stable platform is the last one with the PXI computer and auxiliary batteries which only increased by about 1.7 K. A temperature plot over time can be viewed in *Fig. 25* for the experiment and *Fig. 36* in the appendix for capsule components. Although not visible, the temperature curves in the

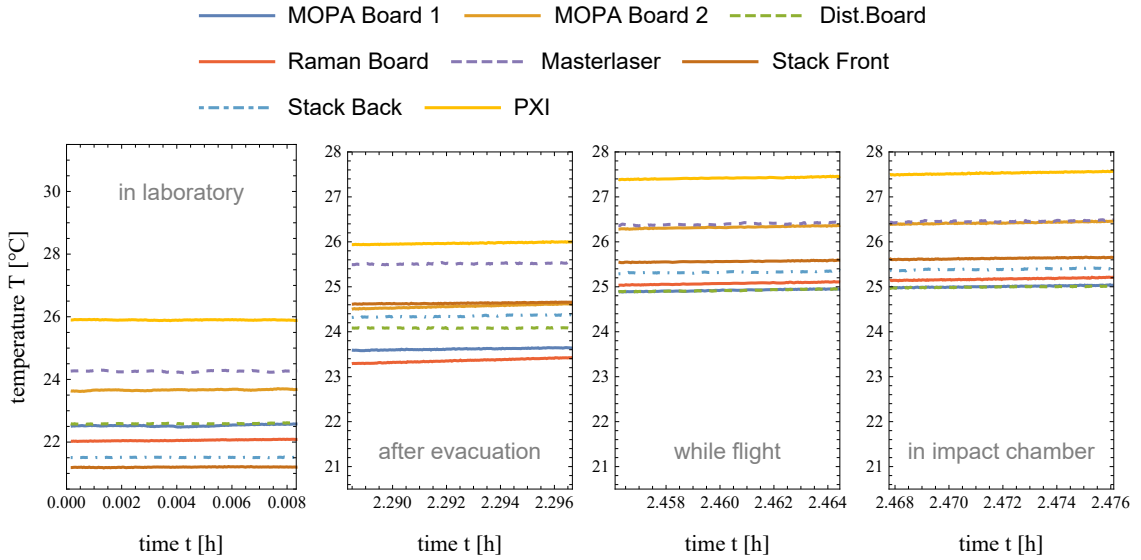


**Figure 25:** Temperatures measured by the NTC sensors on system components in different sequence stages. The respective capsule NTCs are in the appendix in *Fig. 36*

measurements were even higher since all capsule components including the experiment and the internal systems were enabled and running on full power. This lead to a temperature increase of around  $6.4 \text{ K/h}$  and even more during flight with  $7.2 \text{ K/h}$ . Nevertheless this contributes only a small amount (on average  $0.19 \text{ K} \hat{=} 6.2 \%$  compared to  $1.3 \%$  time in the sequence) to the general rise in temperature.

The TBus sensors experience a similar increase of about 4.5 K on the laser current cards and 3.9 K from the power supplies.

Despite temperature rise in the whole capsule, no sign of signal degradation or change in working parameters was seen throughout the whole set of observables.

The temperature controllers monitored the three MOPA laser, the master and the two power amplifier (TA), in the distribution module (VTA) and raman module (RTA) respectively. The temperature over time can be seen in *Fig. 26*. It is visible that the VTA is not stable over the impact event. This is caused by a temporary badly seeded TA due to forces on the optical components whereas slow PID parameters are causing a too slow settling on the target value. These parameters are still

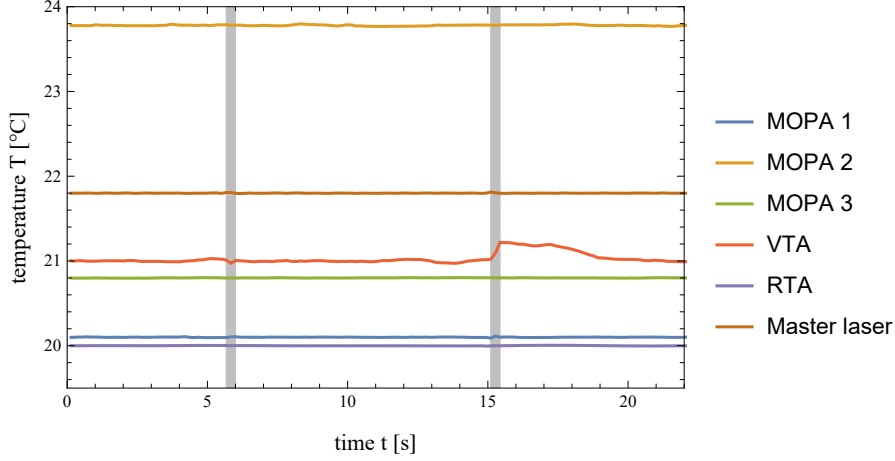


**Figure 26:** TEC temperatures over a catapult sequence. The start and impact are marked with gray bars.

subject to optimization. However, since the start goes nearly unimpeded the system keeps stable over the the curse of flight time. This must still be validated even further because only one flight sequence acquired the whole TEC data stream. This can be done in future drops. We can still say that the TECs are capable enough to withstand the environment conditions in the drop tower and provide fast enough feedback for the laser temperatures.

**Laser performance** The laser performance during flight is an important quality factor for the whole apparatus later on. Stable optical power and frequency are necessary for a fully functioning drop tower experiment with cold atoms. Hence evaluating these properties is of particular interest. Stability can be investigated in two different sub systems: the ability of the MOPA lasers to be offset locked to the master laser, and the reaction of the master itself. The offset beat frequency

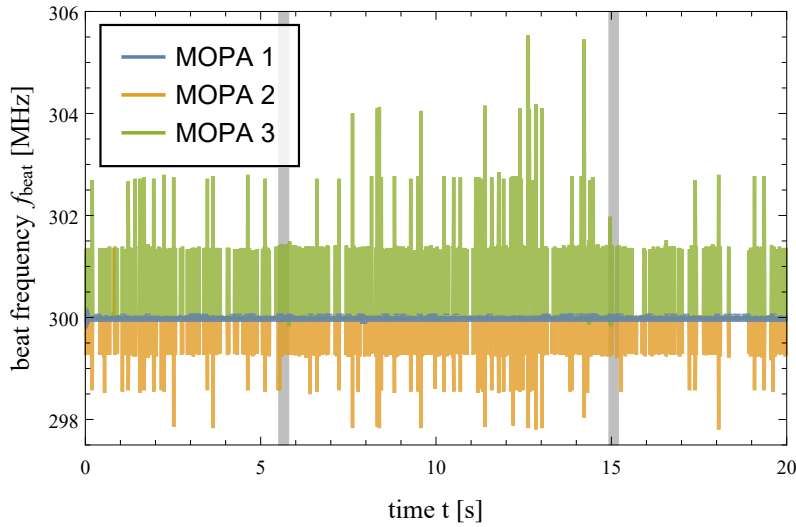


**Figure 27:** MOPA beat frequency during catapult flight. The offset target frequency was set to 300 MHz. It can be seen that the deviations are dominated by digital bit noise. Start and impact durations are marked with gray bars.

is measured and captured by the frequency controller card in the TBus. In **Fig. 27** a typical drop is shown. All three MOPAs here locked on an offset frequency of 300 MHz to the master which is stabilized on the  $^{39}\text{K}$  cross over peak. Thus a nearly sufficient range is covered since the hyperfine niveaus are approximately 83 MHz and 337 MHz away, for  $|F = 1 \rightarrow F'\rangle$  and  $|F = 2 \rightarrow F'\rangle$  respectively in  $^{41}\text{K}$ . It is visible in **Fig. 27** that the lasers were fixed in their offset and are not perturbed by neither the start nor the impact event. The deviations in MOPA two and three

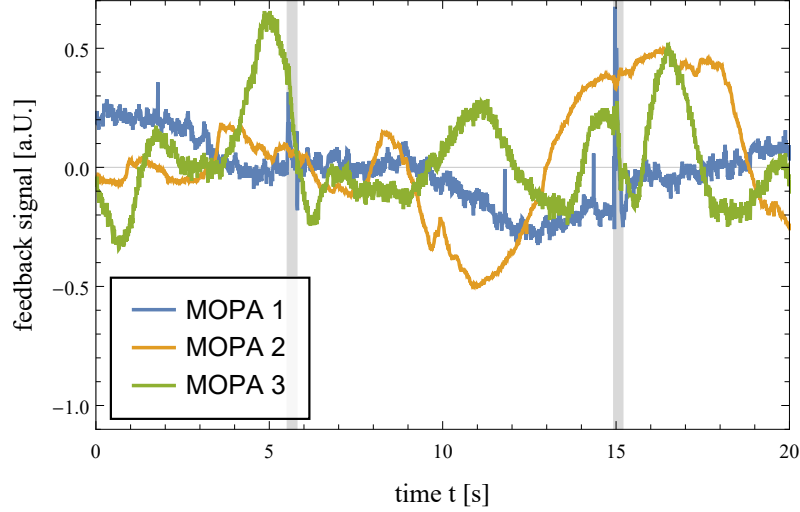


**Figure 28:** Normalized feedback signals of the three MOPA lasers during catapult flight. Start and impact durations are marked with gray bars. The master laser signal can be seen in **Fig. 37** in the appendix.

are bit noise and can be attributed to uncertainties and known electronic issues. Similar information can be seen in **Fig. 28** where the normalized feedback signals are shown. All curves show that the feedback current changed in response to the accelerations. Throughout the measurement, a drift to counteract any frequency changes due to temperature drifts or other effects is additionally visible. Most of them on lie in the second-timescale. The launch and impact effects are visible as sharp, short, small changes in the feedback signals. The master laser shows the exact same behavior (see **Fig. 37** in the appendix).

It thus can be concluded that all MOPA lasers as well as the master kept the frequency stabilization to the desired points in all flights and experiments. No significant deviation or unexpected behavior was measured or seen so far.

**Optical power** To further validate the MOPA performance, the output power must be investigated. The best position for this is behind the lasers since the master oscillator also transmits light in the reverse direction which exits the case at the back. Unfortunately MOPA 3 is blocked by a periscope, so this is only an option for the first two lasers. Looking at **Fig. 29** (*M1 back* & *M2 back*), one can immediately see, that the optical power behind the lasers and therefore the whole MOPA is stable during the catapult sequence (*M1 back* < 8 % and *M2 back* < 0.9 % deviation). (see **Fig. 3** for the diode positions)

However this does not hold for all other measurement points in the system. Immediate next points are the receiving periscopes from all three MOPAS (*M1 periscope*, *M2 periscope* & *Raman periscope*). In all those signals a bit of power (from 10 % up



to a complete loss) is either lost before or after impact. This might be due to the mirror adjustment screws in the periscopes not being fastened enough. For the first laser two other points are measured. Those are fiber end points and would lead the light to the experiment for the 2D MOT and and detection beams. Since the light

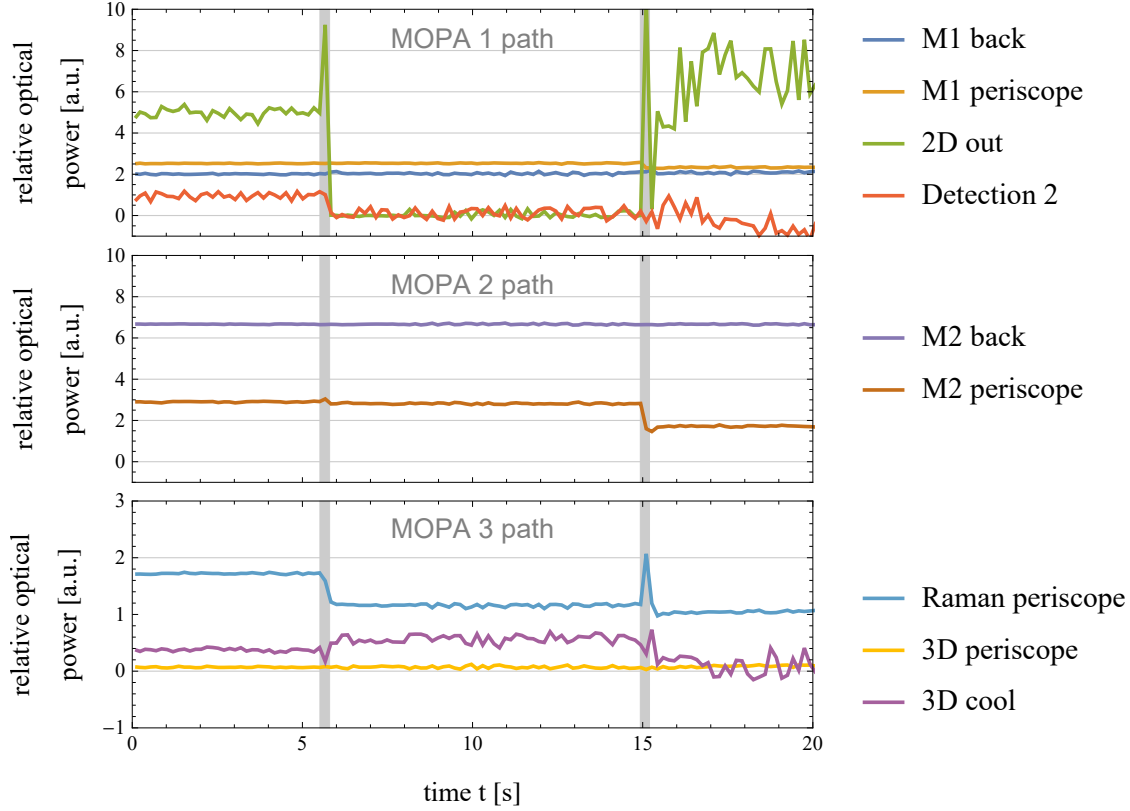


**Figure 29:** Photodiode voltage signals during catapult flight. The three graphs denote diodes in the light path of MOPA 1, 2 or 3 respectively. When diodes are in multiple paths, then only the first occurrence is plotted. The conversion to power was intentionally omitted to keep the relative magnitudes. Start and impact durations are marked with gray bars.

power of those fibers is comparably weak, the highest amplifying setting was used. This seemed to cause noise in the signal but degraded even further while flight and after impact. A similar behavior can be observed for the MOPA 3 path with the *3D cool* out fiber. Although the noise was not so severe like in the fibers mentioned above. This signal was also the only one where the light power has increased during flight. After impact however, the power seems to vanish completely to zero with noise even in the negative values. In later drops it was discovered that the noise seen in the signals (*2D out*, *Detection 2* & *3D cool*) was caused by faulty electronics on the amplifier card. For further flights this was compensated. Additional diodes and reconfigurations were made for the flights number four to six.

Nevertheless the reason for the deviation and changes in the light power on start, flight and impact are up to now not exactly known. Multiple reasons are still being investigated including more electronic issues and calibration problems. The final optical powers for the experiment can only estimated and are still under optimization.

**Capsule rotation** A start in catapult mode induces an rotation onto the capsule. This rotation is measured by a three dimensional gyroscope from the FAB telemetry. Hereby three data streams for every main rotation axes is captured. The  $x$ - $y$  components denote the plane parallel to ground whereas the  $z$  component describes the rotation around the axes in moving direction. The angular velocity  $\omega_i$  around the  $i$  component for a catapult start can be seen in *Fig. 30*. The deviations in the  $x$

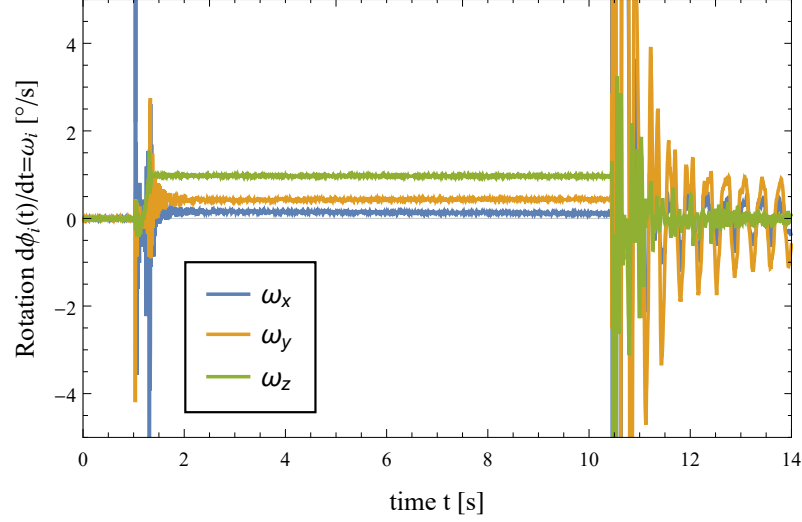


**Figure 30:** Rotations of the capsule over time from a catapult start. A steady angular rotation in the  $x - y$  plane parallel to the velocity vector can be seen as well as for the other two axes.

and  $y$  components stem from minor crooked acceleration vectors from a misaligned mass distribution of the capsule. Although it is calibrated beforehand the center of mass may be off-center with respect to the direction of motion.

To get the whole rotation angles, we can formulate the equation of motion separated in all three axes  $i = \{x, y, z\}$  as

$$\frac{d\phi_i}{dt} = \tilde{f}_t(\omega_{t,i}) \quad (28)$$

where  $\tilde{f}_t(\omega_{t,i})$  describes a linear interpolation in time  $t$  over the discrete angular velocity values  $\omega_{t,i}$ . This can be solved numerically by performing the integration

$$\phi_i(t) = \int_0^t dt' \tilde{f}_{t'}(\omega_{t',i}) \quad (29)$$

with the boundary condition  $\phi_i(0) = 0$ . This could also be formulated in a pure discrete way by accumulating the values multiplied by their respective time differences. The integration of the data in *Fig. 30* is laid out in *Fig. 31*. A depiction of the capsule rotation and axes projections on impact is displayed in *Fig. 35* in the appendix. In general the capsule rotates about  $\overline{\phi_z} \approx 10^\circ$  in the axes parallel to moving direction and with some varying degrees in the other two components.

The oscillating behavior after the deceleration phase is completely ascribable to the impact induced oscillation of the whole deceleration chamber. This can be also seen in video recordings of the impact event.

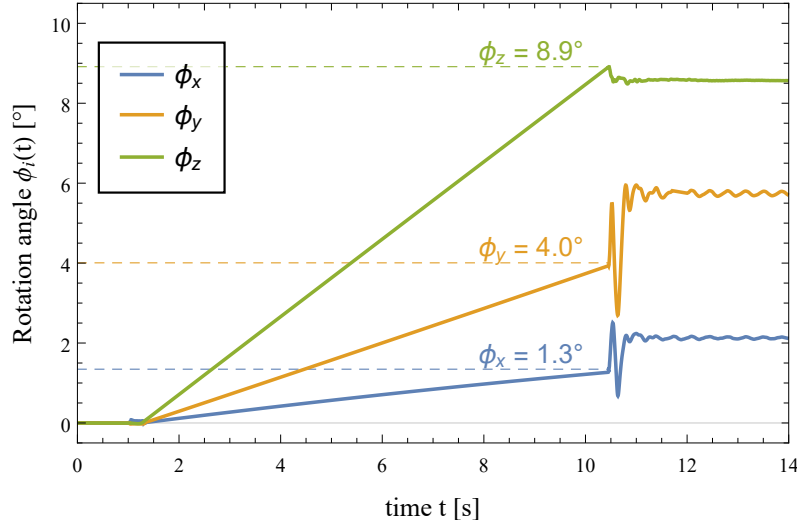


**Figure 31:** Angle of the capsule over time from a catapult start. The steady rotations from *Fig. 30* can be seen to linearly increase the angle over time in all three main axes of rotation. A 3D projection of the angles on impact can be viewed in *Fig. 35*.

### 4.3 Results and conclusions

All in all the system can be seen as partially qualified for its final task of driving potassium based cold atom experiments in the drop tower for QUANTUS-2.

The electronics with the TBus cards are providing a good frequency stabilization for the MOPA and master laser. It is seen that no acceleration or temperature change of up to 4.7 K so far was able to significantly interfere with stability and the feedback signals indicated a sufficient control against any perturbations. The temperature stabilization also worked as desired for all lasers, the master gas cell and optical power amplifiers. Although the TA on the distribution board (VTA) should be configured with faster PID parameters in the temperature stabilization (see *Fig. 26*). Further investigations should also be made for canceling the reason of this impact deviation. One potential cause for the sudden change in temperature at the VTA is misalignment of the seed light into the TA during the catapult shot, as less electrical power will be able to be converted in optical power and has to be dissipated as heat. Stronger tightening of the screws in the coupling mirrors in combination with optimized, faster PID parameters for temperature control could be tested decrease this effect in the future.

The observed capsule rotations did not in any way correlate with important system parameters. Also the reached angles were more than what QUANTUS-2 experiences due to a heavier capsule and the fact that it right now only operates in drop mode. Therefore the system was qualified for more shear acceleration in the  $x$ - $y$  directions, vertical  $z$ -acceleration and rotation in the  $z$  axes than it must withstand in the experiment later on.

The last point to discuss is the stability of the optical power. The only near constant photodiode signals were received by the standing mounts behind the MOPA lasers. This at least proves that the DFB lasers emits a stable power. All other diodes showed a temporary degradation during flight or a sustained change after start and impact. A small part of this can be attributed to tiny changes in the

alignment of the optical elements due to the forces. However a significant amount is still unknown up to this date. The noise seen in the first drops was caused by electronics issues in the transimpedance amplifier card. There might still be other electronic reasons responsible for some of the observed photodiode behavior. It is also noticeable that the standing mounts are not affected by this issue. All other signals were from diodes in laying mounts. This could hint to ground loop problems caused by this component. However, these are only guesses based on the present data and are subject to future evaluations.

In conclusion, it can be said that the system in its current state including temperature stabilization of three MOPAs, two TAs and the master laser, frequency stabilization of three MOPAs and the master laser, data recording and transmission as well as over all experiment procedure has been qualified. While the optical output power measured at the laser diodes was stable throughout the catapult flights, the optical output power stability measured at other points in the system has to be investigated further.

#### 4.4 Future tests

The BLASTEK experiment will continue for a few drops. The qualification will be completed, when the optical powers are being stable during the flight period with small deviations after impact ( $< 10\%$ ) like in the rubidium system. Some improvements are still planned for future use. One is the share of the data capture program in separable pieces. This would enable the asynchronous capturing of the TBus system, the TEC controller and the photodiodes. It also increases the capture rate for the TBus data and the temperature controller independently from each other. It also introduces the need of implementing a proper time synchronization protocol which can be done via internal *tick count* time stamps of the PXI computer. A second improvement is a redesign of the transimpedance amplifier which fixes the noise which is currently avoided by a workaround and may or may not fix the photodiode/light power issues.

A last idea is the implementation of the measurement program as a native program written in c++ or at least parts of it. This would allow for advanced memory management which is not possible in LABVIEW and therefore increase the data capture rate. The FIFO mode could extremely benefit from this. However this approach is a lot harder to maintain and it is unclear if the benefits would outweigh this drawback.

After the BLASTEK target of a stable laser system is reached, the capsule will likely travel back to Berlin to be incorporated in a ground based test environment (*Cold Quanta*, see next chapter for details) to test its capabilities of creating a potassium MOT. After this the system would be able to be integrated into QUANTUS-2 which is estimated to happen in late 2019.

---

## 5 Qualification summary and outlook

### 5.1 Summary of qualification results

**Berlin mini drop tower** The miniaturized drop tower in Berlin provided a sufficient test bed for catapult-capable laser system technology used in cold atom experiments. Although not the entire system was qualified here, the master lasers and temperature controllers as well as the nominal operation of other components were tested. A longtime stability measurement of the master laser was conducted here and the basis of the data capture program were laid.

The principle of an automated frequency stabilization of DFB diodes was successfully shown. Multiple improvements to the older algorithms was made and refined into the new ASAP sampling concept. This will find its application not only in QUANTUS-2 but in future projects and ventures.

An evolutionary algorithm based on swarm optimization was firstly shown to work on PID optimization of temperature controllers. Exploration of possible hyper parameters ranges were explained and an improved new working point provided a sufficient temperature stability for Bremen drop tower operation.

In summary, the mini drop tower was, once again, successfully used as a rapid development facility for various test in high acceleration environment ( $> 30\text{ g}$ ), optimizations, discovery of issues and remedying the latter.

**Bremen drop tower** The Bremen drop tower proved to be a tough environment to cope with in hardware as well as software. The data capture program worked well except for the TEC capturing. Although a direct physical interface seems to be maintained, the connection sporadically breaks off on the start or impact. Because of this only one full data series could be captured on flight number three (see [Tab. 1](#)). This problem has already been narrowed down to the MeCom board which provides the TEC computer interface. However, finding and fixing this fault has not high priority since the temperature controllers are known to work fine in the drop tower mode. Nevertheless this could come into play again in the future when the distribution power amplifier (VTA) gets optimized.

The offset frequency stabilization of the MOPA beat with the master is very reliable and deviations are neglectable as shown in [Fig. 27](#) and [Fig. 28](#). In every drop so far, the lock was maintained. The master laser was also already shown to work reliably on the mini drop tower and the feedback signal (see [Fig. 14](#) (Berlin); [Fig. 37](#) (Bremen, in appendix)) supports this observation.

The optical power for the MOPA lasers is also validated to be constant over a whole catapult sequence. This was shown with the standing mounts on the rear exit. However, all the other measurement points are showing a big degradation of more than ten percent or even a total loss of the optical power signal. Up to date the reason for this is not entirely known and it is still subject to further tests. Potential causes are electronics issues or misalignment of optical paths. Although it is known from the rubidium tests that misalignments occur, it had a small effect of less than 10 % [\[17\]](#). Lastly, accelerations and rotations were shown to be fully absorbed by the system without any damage, so it can be formulated suitable for drop tower operations. When the issue with the optical power is remedied, the whole potassium laser system can then be declared fully qualified. Until then, it is partially qualified.

## 5.2 Outlook

Two findings of this work can not only be applied in QUANTUS-2 but many other experiments and projects using frequency stabilized laser systems. Firstly the autolock procedure. Adaptive sampling was never used before but enabled a much faster time to lock. Also the method for precalculating the reference spectrums for a faster covariance value can be used in future systems. The proposed monte-carlo based approach (ASAP) for an adaptive saturation should be investigated and could yield another way of speeding up the autolock pass.

Secondly the evolutionary optimization. It can help to resolve similar optimization problems for coming issues. It also provides a good test bed for eventual new tasks and application areas. This specifically aims for use in the Berlin BEC ground testbed. Additionally a comparison study can be made with other algorithms like the Nelder–Mead method.

Both advanced studies could be conducted with the BLASTEK capsule in its current state.

### 5.2.1 BLASTEK

BLASTEK so far, reached nearly all goals aimed for. Only small changes for some photodiodes, the transimpedance amplifier and data recording program are planned. The last point to address are the optical power issues. This will be investigated with more flights in the foreseeable future (May 2018 and further). Another idea considered was the use of vibrational tests to faster narrow down the problem. As soon as this is resolved, the capsule can be transported back to Berlin. This marks the point when the potassium laser system is qualified in its principal working mechanisms. For later tests, the shutters could be implemented and controlled but these parts are already drop tower tested from the rubidium system so do not play a critical role. The next logical step is to verify the ability of creating cold potassium atoms in a MOT. This can either be done directly in QUANTUS-2 or a ground based environment testing system.

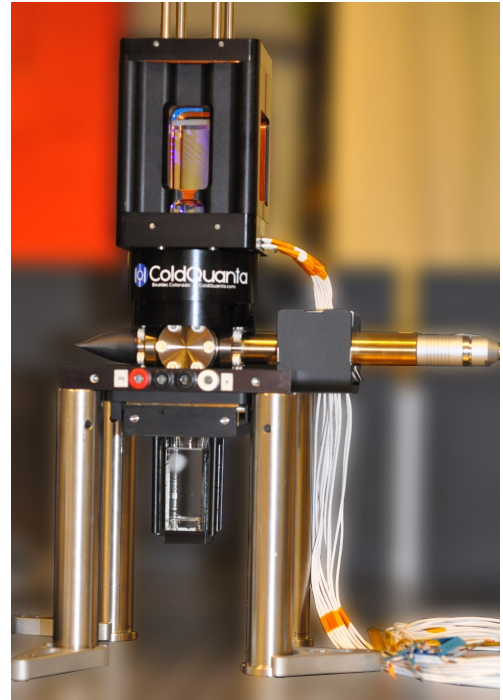


**Figure 32:** Photo of the disassembled RuBECi apparatus as part of the Berlin BEC ground testbed.

### 5.2.2 Berlin BEC ground testbed

RuBECi (see *Fig. 32*) is originally a commercial system for creating dual species Bose-Einstein condensates with alkali atoms in a dedicated atom chip<sup>1</sup>. According to the specifications, it can produce  $^{87}\text{Rb}$ -BECs with a rate of about 1 Hz with approximately  $10^4$  atoms[70]. Although

<sup>1</sup>[coldquanta.com/standard\\_products/rubeci/](http://coldquanta.com/standard_products/rubeci/)

QUANTUS-2 is a lot more effective, with either 30 times the atom number in  $\approx 0.5\text{Hz}$  or the same time but still 5 times more atoms, the system will provide a good testing environment. The system for the Berlin BEC ground testbed was configured without an atom chip and will instead use an optical dipole trap. It will enable the easy testing of a potassium MOT creation and allow to try different sequences and cooling schematics[20, 21]. It would also allow for a reproduction study of Ref. [56] and Ref. [57] with all things learned from the evolutionary TEC optimization.

A successful test here would prove the potassium laser sub system to work and guarantee a full qualification. It also provides a possible tests environment for sub-doppler cooling procedures and optical dipole trapping. It finalizes all system tests and labels the system completely ready for the QUANTUS-2 integration.

### 5.2.3 QUANTUS-2 dual species operation

The integration of the potassium system would need an opening of the vacuum. This is a time consuming process and QUANTUS-2 currently performs some own campaigns with different goals. This includes an investigation of breathing modes for the Rb BEC cloud to determine optimal trap release times and optimization of the magnetic lens for reducing the rate of expansion of the released ensemble.

Taking all factors into account it can be estimated that the potassium system will be implemented in late 2019. Once the system is integrated and cold potassium atoms are created, dual species atom interferometry can be performed in order to yield the first Eötvös ratio  $\eta_{^{87}\text{Rb},^{41}\text{K}}$  measurement in the Bremen drop tower.



---

## 6 References

1. Thiemann, T. in *Quantum Gravity* 41–135 (Springer, 2003).
2. Amelino-Camelia, G., Ellis, J., Mavromatos, N., Nanopoulos, D. V. & Sarkar, S. Tests of quantum gravity from observations of  $\gamma$ -ray bursts. *Nature* **393**, 763 (1998).
3. Lisi, E., Marrone, A. & Montanino, D. Probing possible decoherence effects in atmospheric neutrino oscillations. *Physical Review Letters* **85**, 1166 (2000).
4. Lämmerzahl, C. in *Quantum Gravity* 15–39 (Springer, 2006).
5. Kiefer, C. in *Quantum gravity* 1–13 (Springer, 2006).
6. Damour, T. & Polyakov, A. M. String theory and gravity. *General Relativity and Gravitation* **26**, 1171–1176 (1994).
7. Taylor, B. N. & Thompson, A. *The International System of Units (SI)* tech. rep. (2008).
8. Heavner, T., Jefferts, S., Donley, E., Shirley, J. & Parker, T. NIST-F1: recent improvements and accuracy evaluations. *Metrologia* **42**, 411 (2005).
9. Bloom, B. *et al.* An optical lattice clock with accuracy and stability at the 10-18 level. *Nature* **506**, 71 (2014).
10. Altschul, B. *et al.* Quantum tests of the Einstein Equivalence Principle with the STE-QUEST space mission. *Advances in Space Research* **55**, 501–524 (2015).
11. Kasevich, M. & Chu, S. Measurement of the gravitational acceleration of an atom with a light-pulse atom interferometer. *Applied Physics B* **54**, 321–332 (1992).
12. Peters, A., Chung, K. Y. & Chu, S. Measurement of gravitational acceleration by dropping atoms. *Nature* **400**, 849 (1999).
13. Peters, A., Chung, K. Y. & Chu, S. High-precision gravity measurements using atom interferometry. *Metrologia* **38**, 25 (2001).
14. Von Eötvös, R. Über die Anziehung der Erde auf verschiedene Substanzen. *Math. Naturwissenschaft. Ber. Ungarn* **8**, S65–68 (1890).
15. Touboul, P. *et al.* MICROSCOPE Mission: First Results of a Space Test of the Equivalence Principle. *Physical review letters* **119**, 231101 (2017).
16. Kozuma, M. *et al.* Coherent splitting of Bose-Einstein condensed atoms with optically induced Bragg diffraction. *Physical Review Letters* **82**, 871 (1999).
17. Grzeschik, C. *Experiments with Bose-Einstein Condensates in Microgravity* PhD thesis (Humboldt-Universität zu Berlin, Mar. 2017).
18. Schubert, C. *et al.* Differential atom interferometry with  $^{87}\text{Rb}$  and  $^{85}\text{Rb}$  for testing the UFF in STE-QUEST. *arXiv preprint arXiv:1312.5963* (2013).
19. Szigeti, S. S., Debs, J. E., Hope, J. J., Robins, N. P. & Close, J. D. Why momentum width matters for atom interferometry with Bragg pulses. *New Journal of Physics* **14**, 023009 (2012).
20. Landini, M. *et al.* Sub-Doppler laser cooling of potassium atoms. *Physical review A* **84**, 043432 (2011).

- 
21. Modugno, G. *et al.* Bose-Einstein condensation of potassium atoms by sympathetic cooling. *Science* **294**, 1320–1322 (2001).
  22. Müntinga, H. *et al.* Interferometry with Bose-Einstein Condensates in Microgravity. *Phys. Rev. Lett.* **110**, 093602 (9 Feb. 2013).
  23. Könemann, T. *et al.* A freely falling magneto-optical trap drop tower experiment. *Applied Physics B* **89**, 431–438 (2007).
  24. Van Zoest, T. *et al.* Bose-Einstein condensation in microgravity. *Science* **328**, 1540–1543 (2010).
  25. Gonzalez, D., Seidel, S., Driebe, T. & Rasel, E. *MAIUS 1 – First Bose-Einstein condensate generated in space* (ed DRL.de) [Online; posted 23th January 2017]. Jan. 2017. [http://www.dlr.de/dlr/en/desktopdefault.aspx/tabid-10081/151\\_read-20337/](http://www.dlr.de/dlr/en/desktopdefault.aspx/tabid-10081/151_read-20337/).
  26. Kranz, J. *Aufbau und Charakterisierung eines Lasersystems für Kaliumexperimente im Fallturm* Bachelor thesis (Humboldt-Universität zu Berlin, Feb. 2016).
  27. Schiemangk, M. *et al.* High-power, micro-integrated diode laser modules at 767 and 780 nm for portable quantum gas experiments. *Applied optics* **54**, 5332–5338 (2015).
  28. Tiecke, T. *Properties of Potassium* Appendix A. PhD thesis (University of Amsterdam, 2010). <http://www.tobiastiecke.nl/archive/PotassiumProperties.pdf>.
  29. NIST. *Atomic Weights and Isotopic Compositions with Relative Atomic Masses* <https://www.nist.gov/pml/atomic-weights-and-isotopic-compositions-relative-atomic-masses> (2018).
  30. *6-Slot PXI Chassis for Remote Control NI PXI-1036, NI PXI-1036DC* National Instruments (2014). <http://www.ni.com/datasheet/pdf/en/ds-279>.
  31. *NI PXI-8101/8102 User Manual* National Instruments (June 2010). <http://www.ni.com/pdf/manuals/372800c.pdf>.
  32. *NI R Series Multifunction RIO Integrated Analog and Digital I/O with FPGA Technology* National Instruments (Nov. 2014). <http://www.ni.com/datasheet/pdf/en/ds-98>.
  33. *NI 6259 M Series Data Acquisition: 32 AI, 1.25 MS/s, 48 DIO, 4 AO* National Instruments (June 2016). <http://www.ni.com/pdf/manuals/375216c.pdf>.
  34. *Thermo Electric Cooling Temperature Controller TEC-1091* Meerstetter Engineering GmbH (Nov. 2017).
  35. *XPort Pro* LANTRONIX (2017). [https://www.lantronix.com/wp-content/uploads/pdf/XPort-Pro\\_PB.pdf](https://www.lantronix.com/wp-content/uploads/pdf/XPort-Pro_PB.pdf).
  36. *Ultrafast MSM photodetectors G4176 Series (GaAs)* HAMAMATSU (Mar. 2013).
  37. *Si Photodiode FDS100* Thorlabs (Sept. 2017).
  38. Ruyters, G. & Friedrich, U. From the Bremen Drop Tower to the international space station ISS – Ways to weightlessness in the German space life sciences program. *Signal Transduction* **6**, 397–405. ISSN: 1615-4061 (2006).

- 
39. *Communication Protocol TEC Controller TEC-Family (TEC-1089, TEC-1090, TEC-1091, TEC-1092, TEC-1122, TEC-1123)* Meerstetter Engineering GmbH (Feb. 2017).
  40. *MeCom Protocol Specification* Meerstetter Engineering GmbH (May 2012).
  41. *ADXL150JQC: -5 g to -50 g, Low Noise, Low Power, Single/Dual Axis iMEMS Accelerometers Analog Devices* 0th ed. AD [Analog Devices] (1998).
  42. Allan, D. W. Statistics of atomic frequency standards. *Proceedings of the IEEE* **54**, 221–230 (1966).
  43. Riley, W. *Handbook of Frequency* (NIST, 2008).
  44. Dinkelaker, A. N. *et al.* Autonomous frequency stabilization of two extended-cavity diode lasers at the potassium wavelength on a sounding rocket. *Applied Optics* **56**, 1388–1396 (2017).
  45. Schkolnik, V. *et al.* A compact and robust diode laser system for atom interferometry on a sounding rocket. *Applied Physics B* **122**, 217. ISSN: 1432-0649 (July 2016).
  46. Spindeldreier, C., Wendrich, T., Rasel, E. M., Ertmer, W. & Blume, H. *FPGA-based frequency estimation of a DFB laser using Rb spectroscopy for space missions in Application-specific Systems, Architectures and Processors (ASAP), 2016 IEEE 27th International Conference on* (2016), 207–212.
  47. Roma, N., Santos-Victor, J. & Tomé, J. *A comparative analysis of cross-correlation matching algorithms using a pyramidal resolution approach* 2002.
  48. Hoa, D. K., Dung, L. & Dzung, N. T. *Efficient determination of disparity map from stereo images with modified sum of absolute differences (SAD) algorithm in Advanced Technologies for Communications (ATC), 2013 International Conference on* (2013), 657–660.
  49. Atens, T. *et al.* *Mathematik* 2. korrigierter Nachdruck 2010, 1248–1251. ISBN: 978-3-8274-1758-9 (Spektrum Akademischer Verlag Heidelberg, 2008).
  50. Finch, T. Incremental calculation of weighted mean and variance (2009).
  51. Wörner, L. *et al.* *BOOST: A Satellite Mission to Test Fundamental Physics in Proceedings of the International Astronautical Congress, IAC* (2017).
  52. Barschke, M. F. *et al.* *Optical Quantum Technology in Space using Small Satellites in 68th International Astronautical Congress (IAC). IAC-17, B4, 2, 9, x39017* (2017).
  53. Aguilera, D. N. *et al.* STE-QUEST—test of the universality of free fall using cold atom interferometry. *Classical and Quantum Gravity* **31**, 115010 (2014).
  54. Ziegler, J. G. & Nichols, N. B. Optimum settings for automatic controllers. *trans. ASME* **64** (1942).
  55. Hang, C. C., Åström, K. J. & Ho, W. K. *Refinements of the Ziegler–Nichols tuning formula in IEE Proceedings D (Control Theory and Applications)* **138** (1991), 111–118.
  56. Geisel, I. *et al.* Evolutionary optimization of an experimental apparatus. *Applied Physics Letters* **102**, 214105 (2013).

- 
57. Lausch, T. *et al.* Optimizing quantum gas production by an evolutionary algorithm. *Applied Physics B* **122**, 112. ISSN: 1432-0649 (Apr. 2016).
  58. Bäck, T. & Schwefel, H.-P. An overview of evolutionary algorithms for parameter optimization. *Evolutionary computation* **1**, 1–23 (1993).
  59. Kennedy, J. in *Encyclopedia of machine learning* 760–766 (Springer, 2011).
  60. Fogel, D. B. An introduction to simulated evolutionary optimization. *IEEE transactions on neural networks* **5**, 3–14 (1994).
  61. Scott, D. W. Box–Muller transformation. *Wiley Interdisciplinary Reviews: Computational Statistics* **3**, 177–179. ISSN: 1939-0068 (2011).
  62. Storn, R. & Price, K. Differential evolution—a simple and efficient heuristic for global optimization over continuous spaces. *Journal of global optimization* **11**, 341–359 (1997).
  63. Price, K., Storn, R. M. & Lampinen, J. A. *Differential evolution: a practical approach to global optimization* (Springer Science & Business Media, 2006).
  64. Nelder, J. A. & Mead, R. A simplex method for function minimization. *The computer journal* **7**, 308–313 (1965).
  65. Kelley, C. Detection and Remediation of Stagnation in the Nelder–Mead Algorithm Using a Sufficient Decrease Condition. *SIAM journal on optimization* **10**, 43–55 (1999).
  66. Operation, D. T. & FABmbH, S. C. Z. ZARM Drop Tower Bremen General Information. [https://www.zarm.uni-bremen.de/fileadmin/images/faciliti/pdf/General\\_Information\\_01.pdf](https://www.zarm.uni-bremen.de/fileadmin/images/faciliti/pdf/General_Information_01.pdf) (Apr. 2000).
  67. Operation, D. T. & FABmbH, S. C. Z. ZARM Drop Tower Bremen User Manual. [https://www.zarm.uni-bremen.de/fileadmin/images/droptower/downloads/Users\\_Manual\\_0611.pdf](https://www.zarm.uni-bremen.de/fileadmin/images/droptower/downloads/Users_Manual_0611.pdf) (June 2011).
  68. Liu, G., Guo, L., Liu, C. & Wu, Q. Evaluation of different calibration equations for NTC thermistor applied to high-precision temperature measurement. *Measurement* **120**, 21–27. ISSN: 0263-2241 (2018).
  69. Steinhart, J. S. & Hart, S. R. Calibration curves for thermistors. *Deep Sea Research and Oceanographic Abstracts* **15**, 497–503. ISSN: 0011-7471 (1968).
  70. Farkas, D. M., Salim, E. A. & Ramirez-Serrano, J. Production of rubidium Bose-Einstein condensates at a 1 Hz rate. *arXiv preprint arXiv:1403.4641* (2014).

---

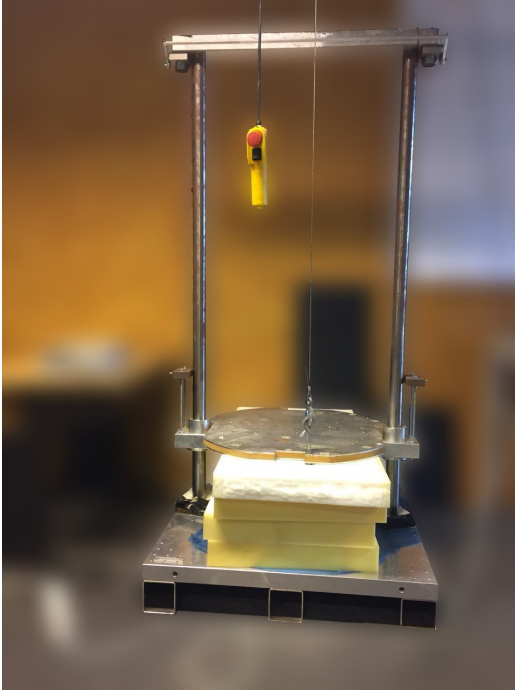
## 7 Appendix

### Equations

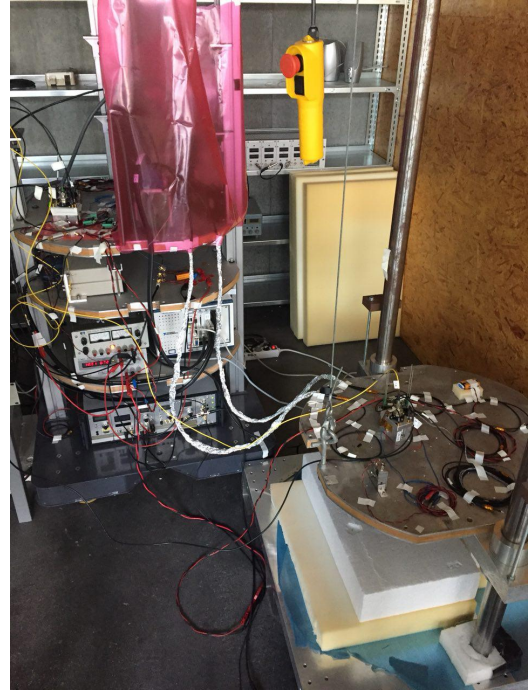
$$\frac{\partial^2 \tau(t)}{\partial t^2} = P(\tau(t) - T(t)) - s \frac{\partial \tau(t)}{\partial t} + r(t, \mu, \sigma) \quad (30)$$

Where  $T(t)$  is the target temperature,  $r(t, \mu, \sigma)$  a random gaussian noise process and  $P, s$  are free parameters to choose. The integrating part can be neglected.

### Figures

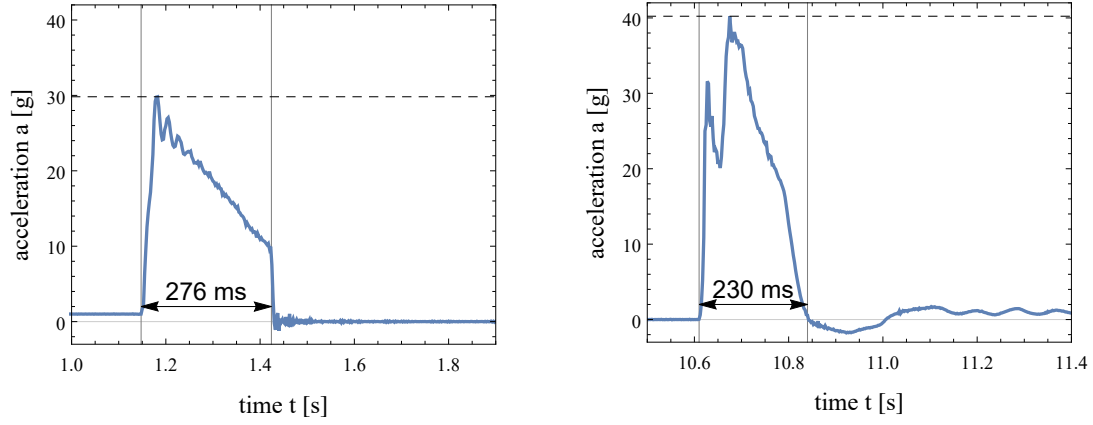


(a) Plain mini drop tower



(b) Mini drop tower with BLASTEK interfacing

**Figure 33:** Photos of the miniaturized drop tower in plain without any additional parts and with BLASTEK running cables to interface the master laser, TECs and the acceleration sensor.



(a) Acceleration peak during a catapult start. (b) Deceleration while capsule impact. The two peaks are caused by the capsule tip geometry.

**Figure 34:** The acceleration peaks while capsule start (left) and impact (right). The time of action is marked and labeled.

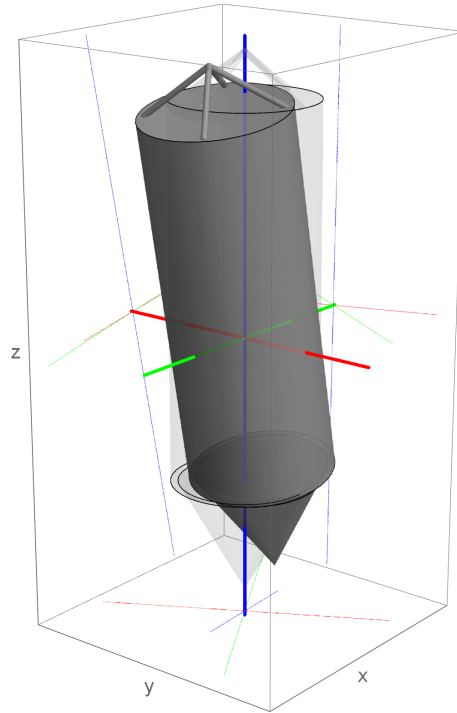


**Figure 35:** 3D rendering of the capsule rotation. The rotation was conveyed with an euler rotation matrix. The angles were three times exaggerated. A projection of the rotated main axes is depicted on the outer planes.

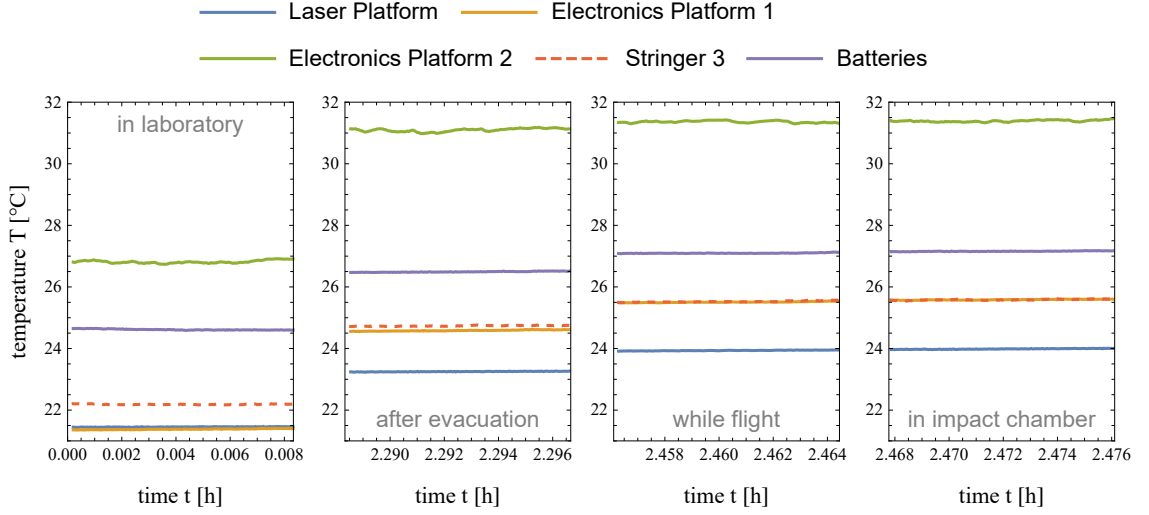


**Figure 36:** Temperatures measured by the NTC sensors on capsule components.

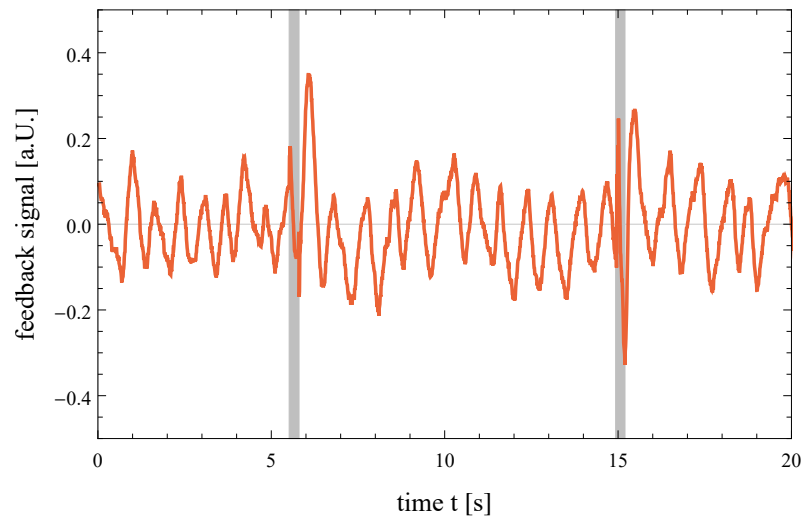


**Figure 37:** Normalized feedback signals of the master laser during catapult flight. Start and impact durations are marked with gray bars. The visible oscillations are mentioned to be due to an unknown electronics issue in the frequency controller card.

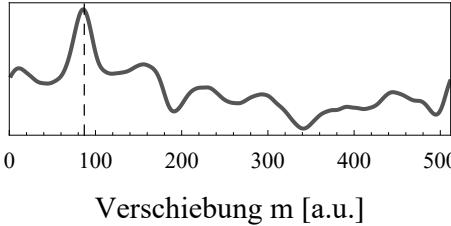
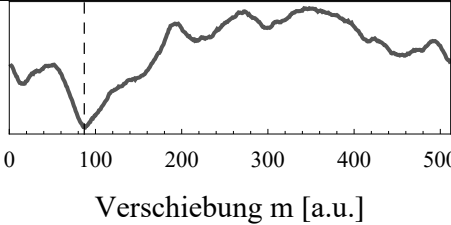
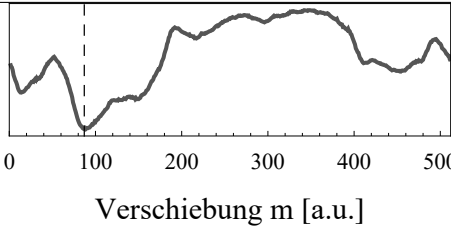
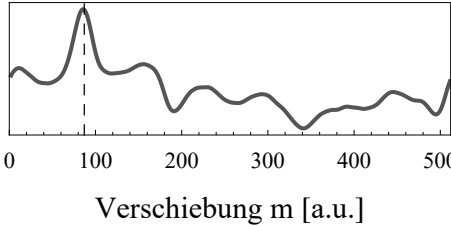


## Tables

**Table 2:** List of all existing and used TBus cards in the BLASTEK experiment.

Card type	Quantity	Task
Interface	1	Communication with the control computer
Power supply	2	Provide necessary supply voltages
Frequency controller	1	Laser frequency stabilization
Current Driver	7	Provide laser currents
Shutter controller	1	Controlling the light shutters
DDS	2	AOM frequency creation
NTC card	1	Read out of the NTC sensors

**Table 3:** Comparison of all investigated correlation like functions for calculating the autolock alignment shift.

Function	Advantages (+) Disadvantages (-)	Typical plot
Cross correlation	+successfully tested in KALEXUS project +statistical interpretation +robust against shifts & noise -comparably slow	
SAD function	+fast +robust against noise -sensitive for outlier	
SSD function	-slower than SAD +robust against noise -sensitive for outlier	
Unscaled cross covariance	+fastest +robust against shifts & noise +possibility for subsequent statistical interpretation	

---

## Algorithms

---

```
 $\vec{x}_{ref} \leftarrow \text{load reference spectrum};$ 
 $\vec{\bar{x}}_{ref} \leftarrow \vec{x}_{ref} - \bar{x}_{ref};$ 
 $m_{trans} \leftarrow \text{load reference transition to lock on};$ 
 $\Delta m \leftarrow \text{load transition threshold};$ 
 $I_{min} \leftarrow I_0 - I_{ctrl};$ 
 $I_{max} \leftarrow I_0 + I_{ctrl};$ 
 $I \leftarrow I_0;$ 
 $s \leftarrow 512;$ 
while  $I_{min} \leq I \leq I_{max}$  do
   $\vec{x} \leftarrow \text{measure current spectrum with } s^{-1} \text{ resolution};$ 
   $\vec{\bar{x}} \leftarrow \vec{x} - \bar{x};$ 
   $m \leftarrow \arg \max_m [(\vec{x}_{ref} \star \vec{x}_{spec})(m)];$ 
   $m_{align} \leftarrow m_{trans} + m;$ 
  if  $|m_{align}| \leq \Delta m$  then
    lock laser;
    break;
  else
     $r \leftarrow \frac{\text{cov}(\vec{x}_{ref}, \vec{x})(m)}{\sqrt{\text{var}(\vec{x}_{ref}) \cdot \text{var}(\vec{x})}};$ 
    if  $r \geq n \sigma$  then
       $\Delta m \leftarrow \text{PID\_state\_machine}(m_{align});$ 
       $\Delta I \leftarrow \xi \cdot \Delta m;$ 
       $I \leftarrow I + \Delta I;$ 
      set current  $I$ ;
       $s \leftarrow f_{adaptive}(m_{align});$ 
    else
      break;
    end
  end
end
```

---

**Algorithm 1:** Simplified outline of the autolock algorithm structure

---

```

 $\vec{p}_{initial} \leftarrow$  load initial parameter set;
 $\vec{p}_{1,...,n_{init.}} \leftarrow \text{mutate}_{1,...,n_{init.}}(\vec{p}_{initial});$ 
 $f_{1,...,n_{init.}} \leftarrow f_{fitness}(\vec{p}_{1,...,n_{init.}});$ 
 $\vec{p}_{1,...,m} \leftarrow \text{select}(\vec{p}_{1,...,n_{init.}}, f_{1,...,n_{init.}});$ 
while program should run do
     $q \leftarrow$  random number in  $[1, m]$ ;
    for  $i = 1, \dots, q$  do
         $qn \leftarrow$  random number in  $\{1, 2\}$ ;
         $\vec{p}_{m+i} \leftarrow \vec{p}_i$ ;
        for  $i = 1, \dots, qn$  do
             $\vec{p}_{m+i} \leftarrow \text{mutate}(\vec{p}_{m+i});$ 
        end
         $f_{m+i} \leftarrow f_{fitness}(\vec{p}_{m+i});$ 
    end
     $r \leftarrow$  random number in  $[1, m]$ ;
    for  $i = 1, \dots, r$  do
         $r_1 \leftarrow$  random number in  $[1, m + q]$ ;
         $r_2 \leftarrow$  random number in  $[1, m + q] \setminus \{r_1\}$ ;
         $\vec{p}_{m+q+i} \leftarrow \vec{p}_{r_1}$ ;
        for  $j = \{1, 2, 3\}$  do
             $rr \leftarrow$  random number in  $\{1, 2\}$ ;
            if  $rr = 1$  then
                 $p_{m+q+i}^{(j)} \leftarrow p_{r_2}^{(j)}$ ;
            end
        end
         $f_{m+q+i} \leftarrow f_{fitness}(\vec{p}_{m+q+i});$ 
    end
    for  $i = 1, \dots, m$  do
        if  $\text{generations alive}(\vec{p}_i) \geq h$  then
             $f_i \leftarrow f_{fitness}(\vec{p}_i);$ 
             $\text{generations alive}(\vec{p}_i) \leftarrow 1;$ 
        else
             $\text{generations alive}(\vec{p}_i) \leftarrow \text{generations alive}(\vec{p}_i) + 1;$ 
        end
    end
     $\vec{p}_{1,...,m} \leftarrow \text{select}(\vec{p}_{1,...,m+q+r}, f_{1,...,m+q+r});$ 
end

```

---

**Algorithm 2:** Simplified outline of the evolutionary swarm optimizing algorithm structure

## Acknowledgements and thanks

*I was told one has to write an acknowledgement. So here we go.  
I thank every person i ever had the joy to interact with and..*

*especially:*

- Markus Krutzik  
*For giving me the opportunity to be part in this whole, insane venture and being a more awesome mentor then I could have asked for.*
- Julia Pahl  
*For dealing with me and my clumsiness in all these months, the pleasure of letting your system fall more than hundred times and the faith that the stuff I did wouldn't break anything.*
- Aline N. Dinkelacker  
*For answering a solid stream of bad questions I had and for sitting with me through seven revisions of my poster. Also, being kind of a second, awesome mentor for me - especially in the last gruesome days of this thesis.*
- Christoph Grzeschik  
*For giving me all the little, detailed, informations whenever i needed them and the joy of trying to write your name without looking it up.*
- Achim Peters  
*For paying all these guys above and giving me the chance to be part of your group for now and hopefully the future to follow the footsteps you left behind for all of us and extend this way even further.*
- Jonas Marschner  
*For including me in your thesis, giving me spiritual support - kind of; and the neverending tale of bad stories you have of me and keeping sure they're never ever getting forgotten.*
- Elke Glaser  
*For guiding me to the decision to study physics.*

*Aline N. Dinkelacker, Christoph Grzeschik, Markus Krutzik, Alyssa V. Mayer and Stefanie Klopp for the insane and invaluable amount of corrections you all provided me.*

*And finally  
my friends, acquaintances, relatives &  
mum, dad **\*wink\***.*

Humboldt-Universität zu Berlin  
Faculty of Mathematics and Natural Sciences  
Department of Physics

Surname	Kluge
First name	Julien
Student ID number	564513

### **Declaration of authorship**

I hereby declare that my bachelor thesis with the title

*Qualification of a laser system for cold atom experiments with potassium in microgravity*

is the result of my own work which has been written only with the help of the indicated sources.

I especially confirm that without any exception, I have fully cited all sources referring to direct quotations of other authors' statements or tables, graphs, quotations as well as all indirect quotations or modified tables, graphics and citations from the internet.

This thesis, in same or similar form, has not been submitted to any other institution.

Berlin, 9th May 2018

Julien Kluge